Extracting Fluid Properties through High-Speed Video Analysis

by

Victoria Allyce Gunning

B.S. Computer Science and Engineering, Massachusetts Institute of Technology (2015)

Submitted to the Department of Electrical Engineering and Computer Science
in partial fulfillment of the requirements for the degree of

Master of Engineering in Electrical Engineering and Computer Science

at the

MASSACHUSETTS INSTITUTE OF TECHNOLOGY

June 2016

Author .....
Department of Electrical Engineering and Computer Science
May 20, 2016

Certified by .....
William T. Freeman
Professor of Electrical Engineering and Computer Science
Thesis Supervisor

Accepted by .....
Dr. Christopher Terman
Chairman, Masters of Engineering Thesis Committee

Extracting Fluid Properties through High-Speed Video Analysis

by

Victoria Allyce Gunning

Submitted to the Department of Electrical Engineering and Computer Science
on May 20, 2016, in partial fulfillment of the
requirements for the degree of
Master of Engineering in Electrical Engineering and Computer Science

Abstract

We explore a non-contact method to measure changes in fluid properties by analyzing refractive motion in high speed video. We present a method of extracting fluid properties by performing video motion analysis using an automated wavelength matching filter followed by fitting of the measurements to theoretical capillary-gravity wave dispersion equations. This method requires an understanding of how field of view, refraction, and parallax affect measurements. We tested the method by analyzing trends in the surface tension to density ratio for cooling water, and for water versus glycerol.

Thesis Supervisor: William T. Freeman
Title: Professor of Electrical Engineering and Computer Science

Acknowledgments

I want to thank Bill Freeman for supervising this project. I wish to acknowledge and thank Katie Bouman, a Ph.D. candidate in the Computer Vision group at MIT, for the tremendous amount of help, involvement, and guidance. I want to thank Miki Rubinstein, a research scientist at Google, for helping advise. I also want to thank Dr. Bales from the MIT Edgerton Center for the equipment access, lab space to perform the experiments, and his contacts P.T. Brun and Luiz Faria in the MIT Mathematics Department for their help in understanding wave behavior. Lastly, I want to thank all my friends from the MIT Physics Department for questioning my measurement methods and helping me navigate the dispersion equations.

Contents

List of Figures

List of Tables

Chapter 1

Introduction

Fluid properties determine how a fluid will behave. It dictates how quickly or slowly something falls through a fluid, how quickly waves propagate through a liquid, and how these differ for different wavelengths. These characteristics determine the behavior of the fluid in given situations [31][27].

The goal of this project is to find a way to measure a fluid's most prevalent properties such as surface tension, density, and viscosity. Most other techniques for measuring these properties are mechanical and rely on contact measurements. Alternatively, I propose to approach this problem non-invasively by taking advantage of the capillary–gravity wave dispersion relation equations. This method allows the surface tension to density ratio and viscosity to density ratio to be measured by analyzing motion at varying frequencies in the video. Analysis of fluid through video would allow these properties to be calculated for fluids in which contamination could be a concern or when touching the fluid isn't a feasible option.

Chapter two describes what fluid's properties are, how dispersion relates to them, previous related work, and advantages for using a camera as a sensor.

Chapter three describes the method and implementation behind extracting the fluid property information from the videos. It details how the videos were collected,

the extraction of the motion signal, and how the observed video was related to the expected theoretical values.

Chapter four describes the details of the experiments. It goes through the calculations behind determining the field of view, and what resolutions are necessary for picking up a discriminative signal.

Chapter five describes the results of the experiments and how they were interpreted.

Chapter six summarizes the results of the project and possible expansions to this work.

1.1 Non-invasive Measurement of Fluid Properties

Established methods used to measure the properties of liquids require contact with the fluid or imposing a constraint as to what kinds of fluids can be studied. For instance, the Du Noüy-Padday is the traditional method for measuring surface tension [19]. It consists of sticking a rod into the liquid and measuring the maximum pull that can be exerted without breaking the fluid's contact. However, there are situations in which the liquid shouldn't be touched for the chance of contamination. Being able to measure these properties non-invasively would allow the liquid to be monitored without introducing foreign contaminants. This could be used to monitor conditions that affect a fluid's properties. Anything from a change in temperature or the introduction of foreign contaminants which both typically alter the surface tension of a fluid. With enough data, this could potential do anything from monitor a patient's blood loss [8] to estimate the temperature of a customer's cup of coffee.

1.2 Using Cameras as a Sensor

With improving technology, cameras have started to replace traditional sensors [38][22][28]. Cameras have the advantage of passively observing their subjects. We can use the information gathered with the camera to extract information visually instead of having to disturb the subject. In addition, cameras are becoming more portable and omnipresent, extending the environments that can be observed [25]. Even though each pixel individually doesn't make a good sensor compared to established methods, by joining all the pixels together a more powerful sensor is constructed that provides spatial resolution which other sensors can't do. As examples, cameras have been used to calculate material properties [14], or reconstruct audio from silent video [15].

Chapter 2

Background

Fluid properties are defining characteristics of a liquid's behavior. The combination of the fluid's viscosity, surface tension, and density determine how waves propagate through the liquid. These can be related using the capillary–gravity wave dispersion relation equations [27].

Since the increased presence of cameras, there are multiple projects that have been using these devices as sensors [22][5][10][15][14][22][35]. There are projects that use cameras to magnify motion, estimate material properties, and extract audio from object vibrations. Each are described in detail in section 2.3.

2.1 Fluid's Properties

This section details the three fluid properties relevant to the capillary–gravity wave dispersion equations, and common methods for measuring these properties. These properties are surface tension, density, and viscosity.

2.1.1 Surface Tension

Surface tension (σ, γ, $\mathrm{mN\,m^{-1}}$) causes the effect where a fluid has the tendency to occupy the smallest surface area. The cohesive forces between the liquid's molecules cause them to be pulled towards adjacent molecules. Since molecules at the surface have fewer similar molecules to bond to, due to the air-liquid interface, they exhibit a stronger pull on their neighbors than their fully-submerged counterparts.

Surface tension can be measured as the amount of force required to break a film of length 1 cm, or energy per unit area. There are also several factors that can decrease a fluid's surface tension one example is impurities. For instance, dust and other impurities in tap water decrease surface tension.

There are several ways to measure surface tension [19][20][30]. The standard methods generally consist of the du Noüy ring method which measures the maximum pull that can be exerted on the ring without breaking the fluid contact. This is done by touching the ring to fluid and then pulling the ring away from the liquid. The force needed to break the contact between the ring and the fluid gives a surface tension measurement. The Du Noüy-Padday is a slightly simplified method which uses a rod or needle instead of a ring [23].

2.1.2 Density

Density (ρ, $\mathrm{kg\,m^{-3}}$) is the mass over the volume [2]. A simple way to calculate this is to take a graduated cylinder and measure the weight and volume of the fluid [16]. Typically, density is changed by changing either temperature or pressure. However, for liquids and solids, changes in density tend to be small because most liquids and solids require a change of hundreds of degrees Celsius to increase or decrease density by one percent.

2.1.3 Viscosity

Viscosity (η, μ, $\mathrm{kg\,s^{-1}\,m^{-1}}$, ν, $\mathrm{m^2\,s^{-1}}$) is the resistance of a fluid to gradual deformation by shear or tensile stress. A higher viscosity equates to a thicker fluid and higher resistance to stress. There are two kinds of viscosities, dynamic and kinematic. Dynamic viscosity (η, μ) is the resistance of the fluid to shearing flow. Shearing flow is when layers of the fluid would be move with different speeds. The kinematic viscosity (ν) is the ratio of the dynamic viscosity to the density of the fluid [17].

The standard lab equipment for viscosity is generally either a U-tube viscometer [9] or a falling sphere viscometer [7]. The U-tube viscometer measures the viscosity by calculating the time it takes for the fluid to travel between two marks on the tube. Each tube type has its own conversion factor to calculate the kinematic viscosity from this method. The falling sphere method uses Stokes' law to calculate the viscosity by knowing the size and density of the sphere that falls through the liquid, the density of the liquid, and terminal velocity of the sphere in the liquid [13].

Viscosity tends to be strongly dependent on temperature, and is independent of pressure except for exceptionally high pressures. Viscosity generally decreases, fluidity increases, as temperatures increase [32].

2.1.4 The Effect of Temperature on a Fluid Properties

As temperature increases, most fluids will decrease in density. As the molecules tend to move they occupy more space while maintaining the same weight [2]. For surface tension, the general trend is that it decreases with the increase of temperature [12]. For viscosity, the fluidity tends to increase with temperature meaning the viscosity decreases with decreased temperature [32]. The interaction between the molecules contain more energy with these behaviors. The intermolecular forces influence each other less, and the molecules spread out more. This theoretical behavior of water affected by varying temperature is shown in section 2.1.4.

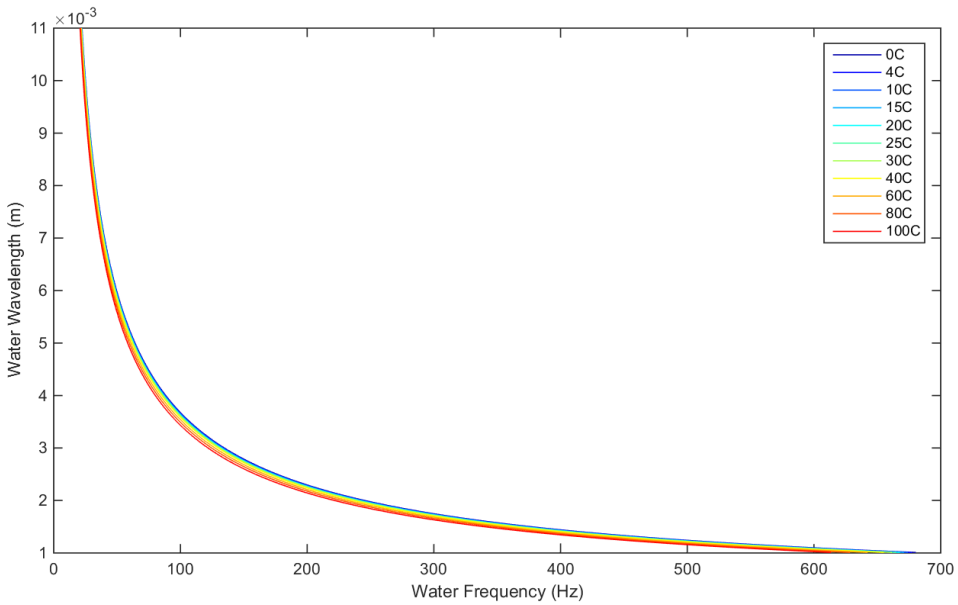

Figure 2-1: The expected wavelengths at different frequencies for different temperatures of water in Celsius. Blues correspond to colder and reds correspond to warmer water temperatures. The temperatures range from 0°C to 100°C.

2.2 Dispersion

Dispersion is what happens different wavelengths propagate through a medium at different speeds. In the case of fluids, when the wavelengths are large the velocity of the wave will depend on gravity. When the wavelengths are short the velocity of the wave will depend on the fluid's properties [27]. This same effect is observed when splitting light through a prism. The white light is comprised of many wavelengths and each wavelengths travels through the prism at a different speed [18].

The behavior of waves in a fluid depends on the fluid's properties. The proposed way to calculate the fluid properties is to extract information about the wave behavior. Dispersion with capillary–gravity waves is a well-studied wave–fluid interaction that depends on the fluid's properties [4][21].

There are two major restoring forces when observing waves in a fluid. There are forces from gravity which are the major restoring factor in larger wavelengths, and there are capillary forces which are the major restoring forces in smaller wavelengths. These waves are called capillary–gravity waves and by knowing the velocity of each of these waves the fluid's properties can be estimated using established dispersion equations.

When the predominant restoring force in the waves is due to capillary effects, the dispersion relation equation includes the influences of surface tension, density, and viscosity in the propagation speeds of waves through the fluid. In larger wavelengths, these effects are negligible compared to the forces of gravity on the surface wave. Because of this, measurements must capture smaller wavelengths (capillary waves).

2.2.1 Capillary–Gravity Waves

In order to measure these properties, capillary waves are often created using wind passing over the fluid or vibrations propagating through the fluid.

There are some well-studied solutions to the capillary–gravity wave dispersion equations where the waves are generated using a single force. Faraday waves are an example of this; the waves are generated using a vertical driving force on a thin bath of the fluid. The waves created are then related to the driving frequency of the vertical piston and dependent on the properties of the fluid [34].

Dispersion Relation

The dispersion relation for capillary–gravity waves has many forms depending on the constraints and boundary conditions. The full equation is found in [4] and [27] is

$$(i\omega + \frac{2\eta k^2}{\rho})^2 + gk + \frac{\sigma}{\rho}k^3 = \frac{4\eta^2 k^3}{\rho^2}(k^2 + i\omega\frac{\rho}{\eta})^{\frac{1}{2}} \tag{2.1}$$

where η is the viscosity, ρ is the density, k is the complex wave factor, $k = k_0 - i\alpha$ where $k_0 = \frac{2\pi}{\lambda}$, g is acceleration due to gravity, ω is angular frequency and σ is surface tension. α is the attenuation coefficient.

There are some approximations that are accurate in the capillary limit when there are extremely large values of k You can assume that $\omega\frac{\rho}{k^2\eta} >> 1$ giving a new equation.

$$(k^2 + i\omega\frac{\rho}{\eta})^{\frac{1}{2}} \approxeq (1+i)(\omega\frac{\rho}{2\eta})^{\frac{1}{2}} \tag{2.2}$$

From this you can derive ω^2 to be

$$\omega^2 = gk + 4iw\frac{\eta}{\rho}k^2 + \left[\frac{\sigma}{\rho} - (1+i)\frac{\omega^{\frac{1}{2}}2^{\frac{3}{2}}\eta^{\frac{3}{2}}}{\rho^{\frac{3}{2}}}\right]k^3 + 4\frac{\eta^2}{\rho^2}k^4 \tag{2.3}$$

Then you can substitute values for k. After substitution, you can separate out the real and imaginary portions of the equation and derive the following relationship. The effects from the fluid's properties are isolated in the brackets.

$$\omega^2 = gk_0 + \left[\frac{\sigma}{\rho} - \sqrt{8\frac{\eta^3\omega}{\rho^3}} + 4k_0\frac{\eta^2}{\rho^2}\right]k_0^3 \tag{2.4}$$

This equation can be simplified to ignore the effects of small viscosities to by taking the limit as η approaches 0.

$$\omega^2 = gk_0 + \frac{\sigma}{\rho}k_0^3 \tag{2.5}$$

By plotting a $\frac{\omega^2}{k_0}$ vs k_0^2, the relationship between density, surface tension, and viscosity is demonstrated by the slope of the line eq. (2.6) or the curve produced eq. (2.7). If it's a line, then the slope is $\frac{\sigma}{\rho}$. If a curve is produced, it is because a high viscosity will dominate the higher frequencies with the $\eta^{\frac{3}{2}}$ causing a downward turn. An example plot is given from [4] in fig. 2-2.

$$\frac{\omega^2}{k_0} = g + \frac{\sigma}{\rho}k_0^2 \tag{2.6}$$

$$\frac{\omega^2}{k_0} = g + \left[\frac{\sigma}{\rho} - \sqrt{8\frac{\eta^3\omega}{\rho^3} + 4k_0\frac{\eta^2}{\rho^2}}\right] k_0^2 \tag{2.7}$$

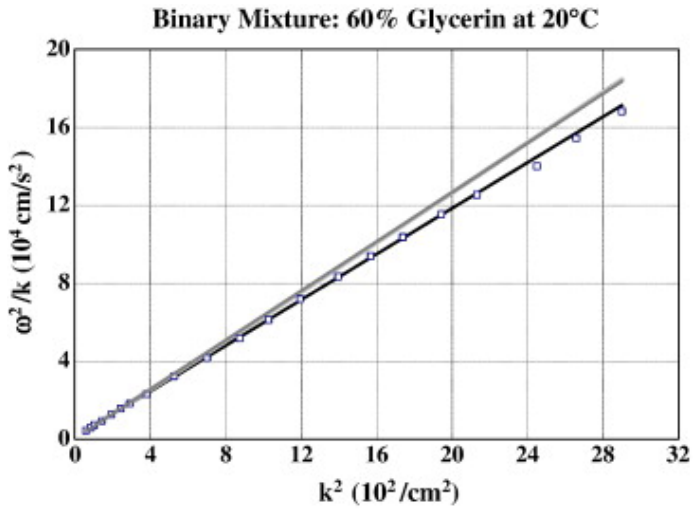

Figure 2-2: Dispersion data for capillary waves plotted as $\frac{\omega^2}{k_0}$ vs. k_0^2 for the binary mixture with 60% glycerin at 20°C. The solid line is a fit using a modified version of dispersion eq. (2.4). The gray line is a fit using the simplified equation, which does not take the effect of viscosity into account eq. (2.5). Figure taken from [4].

Group Velocity and Phase Velocity

When observing waves propagating through a liquid, there are two velocities. The phase velocity, v_p, is the speed at which a single wavelength propagates through the fluid. However, when a fluid is excited, there is a bandwidth of frequencies that are excited, and multiple wavelengths traveling through the medium. This leads to another velocity, the group velocity, v_p, that describes the velocity of the envelope.

The group velocity can be described as the change in angular frequency over the change in wave number eq. (2.8), and is the observed result of combining all the excited waves [6][29].

$$v_g = \frac{\partial\omega}{\partial k} \tag{2.8}$$

The phase velocity of an individual frequency or wave is $v_p = \frac{\lambda}{T}$ or $v_p = \frac{\omega}{k}$. Which can be solved for from the group velocity by integrating eq. (2.9).

$$\omega = \int v_g \partial k \tag{2.9}$$

When approaching the limits of either pure gravity or pure capillary waves, the ratio of $\frac{v_g}{v_p}$ is $\frac{1}{2}$ and $\frac{3}{2}$ respectively. The derivations can be seen in appendix C.1.

In Practice–Ignored Effects

This project's experimental setup can ignore a few terms. The following eq. (2.10) shows the dispersion relation assuming that viscosity, surface tension, density, and the depth of the fluid all have effects on the speed waves travel in the liquid. The influence of the depth of the fluid can be seen with the tanh term.

$$\omega^2 = \left(gk_0 + \left[\frac{\sigma}{\rho} - \sqrt{8\frac{\eta^3\omega}{\rho^3} + 4k_0\frac{\eta^2}{\rho^2}} \right] k_0^3 \right) \tanh(k_0 h) \tag{2.10}$$

Viscosity When studying water or other low viscosity (high fluidity) fluids, the effects of can be ignored. This is the effects viscosity aren't noticeable under 5kHz [4]. This is because the two terms influenced by viscosity in eq. (2.4) are relatively small and cancel each other out at these lower frequencies. Viscosity is considered sufficiently small with eq. (2.11). This gives eq. (2.12).

$$\nu k_0^2 \ll \omega^2 \tag{2.11}$$

$$\omega^2 = (gk + \frac{\sigma}{\rho}k^3) \tanh(kh) \tag{2.12}$$

Depth When looking at surface waves, there are two general conditions. Either the waves are in shallow or deep liquid. When the fluid is sufficiently deep and there

are deep waves, the $\tanh(kh)$ goes to 1 simplifying the equation to eq. (2.5) without the effects of viscosity and eq. (2.4) with the effects of viscosity. Shallow water is when the depth of the water is not sufficient for the tanh to approach 1 and affects both the phase and group velocities of the waves. An example boundary for shallow versus deep water is shown in fig. 2-3 for varying depths and wavelengths.

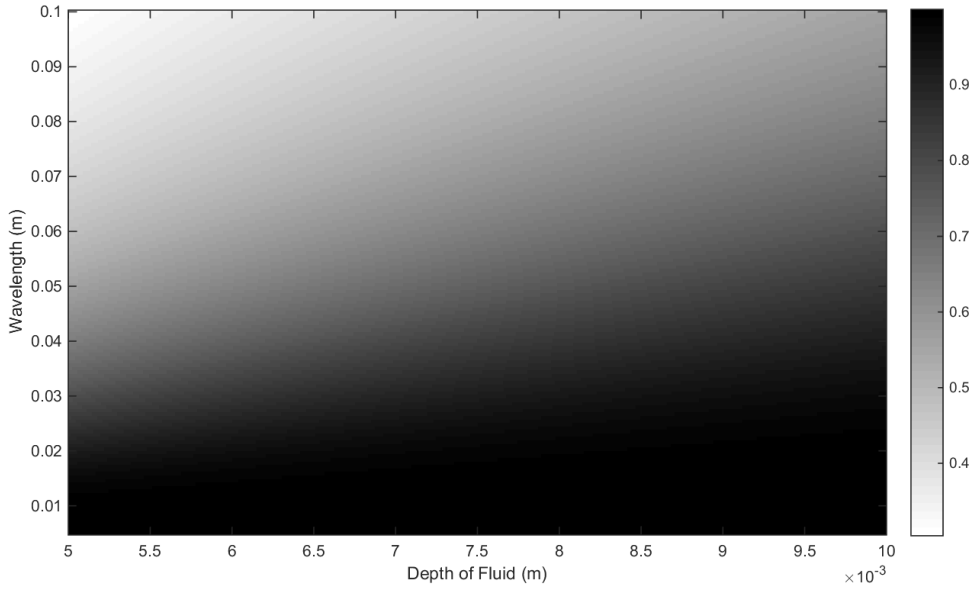

Figure 2-3: The shallow versus deep water boundary for water depths from 0.5cm to 1cm for wavelengths 10cm to 0.5cm. This means a ratio of 20× to $\frac{1}{2}$×
. Black indicates deep water, white indicates shallow water.

Boundary Conditions Depending on the constraints of a system, the capillary–gravity wave dispersion equations may depend on the size of the container due to boundary effects [21]. These boundary conditions appear when the container is smaller than 10λ (isn't larger by at least an order of magnitude).

All of these equations assume there are minimal effects due to boundary conditions from the container. This is generally assumed with the wavelength observed is and order of magnitude smaller than the size of the container.

2.2.2 Previous Work Using Dispersion to Measure Fluid Properties

A non-contacting technique for measuring surface tension of liquids[11]

The work proposed in [11] used dispersion relations to measure surface tension by using a 48-mm focal length 3MHz ultrasonic transducer. They were able to generate small waves at the surface of the water. A specialized microscope which uses a photodiode and a photodetector behind a pinhole to measure the variation in intensity of the light reflected off the surface of the water was then used to measure the surface tension of the liquid. The variation in intensity of the light can be related to the surface height variation in the fluid.

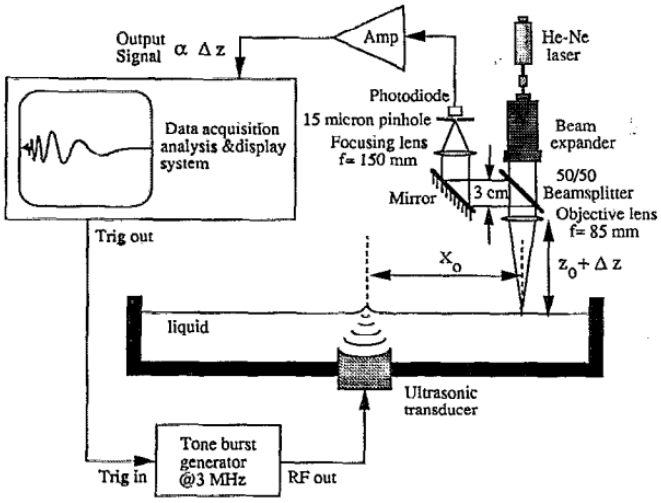

Figure 2-4: The schematic of the capillary wave generation and detection system taken from [11].

Assuming a known density, this method can solve for the surface tension of fluids with low viscosity by using a simplified version of the dispersion equations. They solve the simplified dispersion equations by limiting the number of variables in their system; they take measurements at one point, and they know the distance between

the wave source and the point being analyzed by the microscope. They then analyze a point of the surface at a known distance from the wave source and use FFT on the wave profile observed at a point to calculate the surface tension.

$$FFT[g(x_0, t)] = G(\omega) \exp^{j\phi(\omega)} \tag{2.13}$$

$G(\omega)$ and $\Phi(\omega)$ are the amplitude and the phase of $g(x_0, t)$ and x_0 is the distance between the excitation point and the detection point. $\Phi(\omega) = kx_0$. Kelvin's dispersion equation for deep water approximations, $\tanh(kh) \cong 1$, gives an equation for surface tension as

$$\tau = \frac{x_0^3 \rho \omega^2}{[\Phi(\omega) + \Phi 0]^3} - \frac{x^2 \rho g}{[\Phi(\omega) + \Phi 0]^2} \tag{2.14}$$

This method ignores the effects of viscosity. They acknowledge that these effects can be corrected for by taking measurements at two places in the fluids and calculating the damping effects. Although taking multiple measurements more computationally involved, it can reveal more information about the fluid's properties.

Effect of viscosity on dispersion of capillary–gravity waves[4]

This study generates waves by creating an alternating electric field between a blade and the fluid. In polar fluids that they're studying, the alternating electric field generates tiny surface waves. Subsequently because the surface waves are small wavelengths one can simplify the dispersion equations to assume deep fluid boundaries.

To analyze the wave behavior, they used a laser and detected the interference signal. The surface wave was recovered through analysis of the interference pattern. They used this pattern to measure the wavelengths of the surface waves at different frequencies in water and glycerin mixtures. Then, they used this information to solve for the surface tension to density ratio and viscosity to density ratios in the dispersion equations. The main restriction is that these methods require polar fluids

in order to work since they create the capillary waves in their experiments through the use of an alternating electric field. As of such, they limited their experiments to water and glycerin mixtures since both molecules are polar.

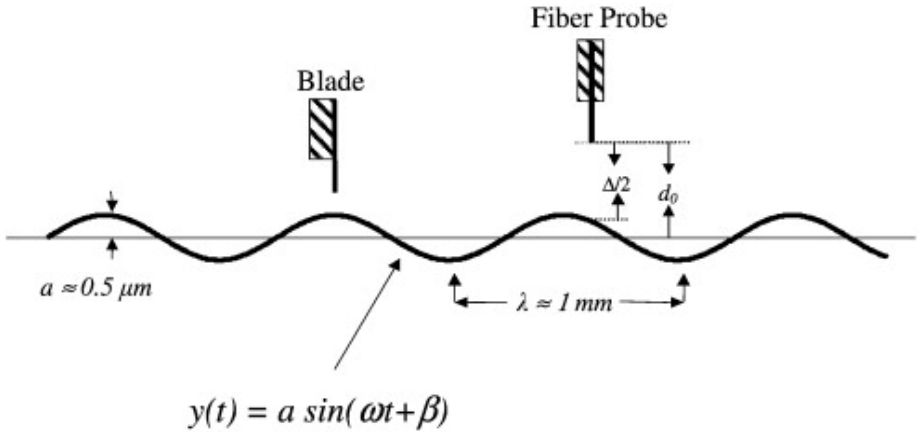

Figure 2-5: The schematic of the wave generating blade over the fluid. This works in polar fluids because they are affected by the electric field. Figure taken from [4].

2.3 Cameras as a Sensor

Cameras have become more portable and prevalent in society, and the places where they are used as sensors is increasing [25]. With improvement in technology, it has become easier to replace traditional sensors with cameras. Even though each pixel in the camera individually is a bad sensor, the combined whole gives a matrix providing spatial information. Additionally, cameras have the advantage of passively observing their subjects. The information gathered with the camera is extracted visually instead of needing to disturb the subject.

2.3.1 Phase-Based Video Motion Processing[37]

By using complex-value image pyramids, this work extracts tiny, sub-pixel motion from video, and then magnifies the video. The coefficients of the phase variations in the pyramid over time are temporally processed and amplified to magnify motion at a specific range of frequencies.

Small motion in a local region of the image can be represented by the original image region with a displacement $f(x + d(t))$. When this is modeled using a Fourier series decomposition, the displacement becomes part of the phase information.

$$f(x + d(t)) = \sum_{\omega=-\infty}^{\infty} A_\omega e^{i\omega(x+d(t))} \tag{2.15}$$

To amplify this motion, [37] uses a temporal filter to remove the DC component corresponding to the original position leaving us with only the phase component eq. (2.17). This can be multiplied by a constant (α in this paper) to amplify the original motion. This is then done in sub-bands eq. (2.16) and collapsed to generate the motion magnified video shown in eq. (2.18).

Each sinusoid in eq. (2.15) corresponds to a single frequency ω as in eq. (2.16).

$$S_\omega(x, t) = A_\omega e^{i\omega(x+d(t))} \tag{2.16}$$

The motion encoded in $\omega(x + d(t)))$ is then filtered with a DC balanced filter to give eq. (2.17).

$$B_\omega(x, t) = \omega d(t) \tag{2.17}$$

Afterwards, the phase multiplied by an amplification factor α to increase the motion. By recombining all subbands, the resulting motion magnification is eq. (2.18).

$$\hat{S}_\omega(x, t) = A_\omega e^{i\omega(x+(1+\alpha)d(t))} \tag{2.18}$$

This project uses this process to visually inspect the motion at varying frequencies. In addition, temporal filtering can be used to extract motion at specific frequencies. Both of these techniques are useful for this project's work extracting the fluid's wavelengths at specific speeds corresponding to frequencies.

2.3.2 Visual Microphone: Passive Recovery of Sound from Video[15]

In this paper, the authors use high-speed video to extract tiny vibrations which are used to reconstruct the sound which caused the vibrations. They visualize the spatial motion by doing a Fourier transform on the video. In this domain, the phase difference between the waves at individual frequencies corresponds to the direction of motion. Though localization, the motion of regions is extracted. For visualization, they encode the phase with hue and magnitude with saturation. An example of this is found in both [14] and [15] and shown in fig. 2-6.

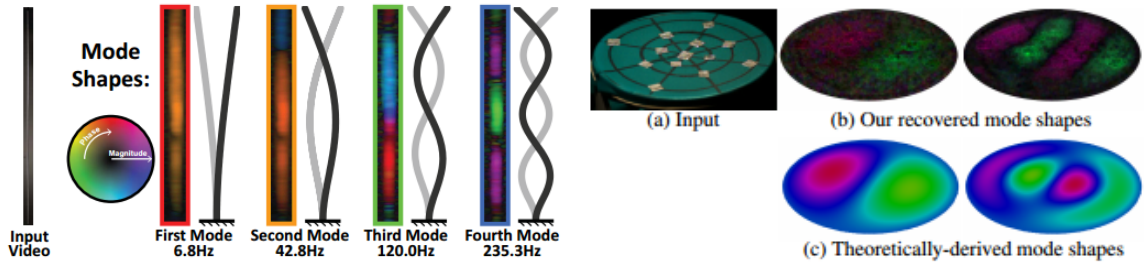

Figure 2-6: Motion visualization through phase and magnitude color coding. The figure on the left is taken from [14] and the right is taken from [15]. The hue corresponds to the direction of the motion or phase, and the saturation corresponds to the magnitude of the motion.

2.3.3 Visual Vibrometry: Estimating Material Properties from Small Motions in Video[14]

In this paper, material properties can be extracted by analyzing the shapes and frequencies that the material vibrates at. They extract information about fabrics and rods by studying the frequencies and shapes of the material's natural modes as shown in fig. 2-6.

Fluids don't behave in the same way as solid objects, and thus these methods can't be extended to them. However, similar to [14], extracting spatial information about a fluid's behavior yields information about the fluid's properties.

2.3.4 Estimating the Material Properties of Fabric from Video[5]

The authors show that they can recover trends in fabric properties by analyzing motion of fabrics under unknown wind forces. The behavior of the fabric motion is influenced by the fabric's properties. To do this, they extracted the magnitude of the motion using optical flow and extract features from this representation of motion that are then used to train a fabric property classifier. The frequencies of the motion was further broken down into sub-bands and simplified using PCA to reduce the dimensionality of the problem.

2.3.5 Refraction Wiggles for Measuring Fluid Depth and Velocity from Video[39]

This paper uses intensity variations over a textured dot pattern background to extract the velocity and 3D location of a refractive fluid between the camera and background. The variations which they call "refraction wiggles" are features which they can track to recover the fluid motion and location.

In fluids, the refraction is determined by the refractive index and determines

how much the background is distorted by looking through the fluid. As a wave is propagating across the surface of a fluid, the wave acts like a lens and will bend the light based on the ratios of the refractive indexes between the mediums and the angle of entry or exit. The light will bend depending on the angle that it enters the fluid. When there are waves, the angle of the light changes based on the position the light is entering or exiting the waveform above. It will shift the background deforming it based on that shape. Like in this work, the waves observed will move across the liquid creating similar deformations on the background.

Chapter 3

Method

When viewing the bowl of liquid with a top-down viewpoint, a wave of a specific wavelength travels along the surface of a fluid at a frequency related to its wavelength. Refractive effects will cause an image below the bowl to distort, and a single wavelength moving will cause points to wiggle at a frequency related to the wave speed. As multiple waves are excited a bandwidth of frequencies propagate and disturb the surface of the water, the resulting motion of the background behind the surface of the fluid is composed of the combined motion of each propagating wave. By placing a dot pattern as a background, sub-pixel information can be gathered about the localized relative motion of the dots.

Assuming that the dot pattern will move with the same frequency as the wave propagating through the water, the expected motion can be calculated using the dispersion equations and used for setup calculations. The conversion between speed and angular frequency for a specific wavelength is further explained in section 3.3.1.

To experimentally calculate the fluid properties, the reverse should be possible. If the individual spatial frequencies that the dot is moving at are found for the corresponding temporal frequencies, then the wavelength and propagation speeds should be able to be related to the dispersion equations. By breaking down the

motion of the dots into their respective frequencies using a Fourier transform, the wavelengths and the speed which they are traveling across the fluid can be fit to the expected response of the capillary-gravity surface wave dispersion equation.

3.1 Overview

The processing pipeline for a set of videos consists of:

1. Setting up and collecting the high-speed videos
2. Uploading and performing motion analysis, acquiring the localized minute motion in each video
3. Doing an FFT on the motion
4. Using a match filter on each temporal frequency to measure the wavelengths (spatial frequency)
5. Fitting the capillary–gravity waves dispersion relation to the match filter response

To present the proposed pipeline, the process for a 1D wave traveling over a surface is explained. In this toy example, the background is a column, line, of pixels. As the wave travels over the surface, it changes the relative position of each pixel. This is mapped out in fig. 3-1 for a whole period of the wave from the initial view beneath the wave through a full period. If there was interference from multiple waves, the result may look like fig. 3-2. When more complex motion is broken down using an FFT, each resulting component of motion will be referred to as the temporal frequency of the motion, temporal slice, or slice of motion.

The amplitude of the wave corresponds to the amplitude of the local motion. This means that experiments should be taken with a preference towards smaller amplitude

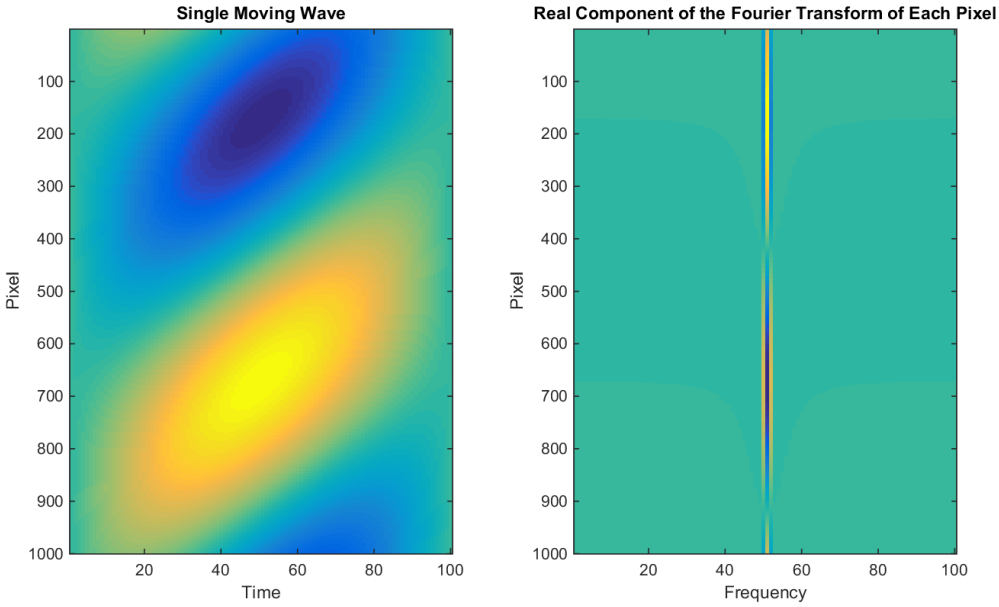

Figure 3-1: On the left, the displacement of a given column of pixels is mapped out as a wave disturbs the observed position. The wave travels one full wavelength (period) in the 100 time steps. On the right is the resulting FFT with the DC component spike in the center, the imaginary portion on the left, and the real portion on the right. The frequency of the motion from the FFT is one column away from the center showing that it has one cycle over the duration of movement. The spatial frequency (column of the FFT) matches the displacement modeled by the left side. The signal ranges from 1 to -1.

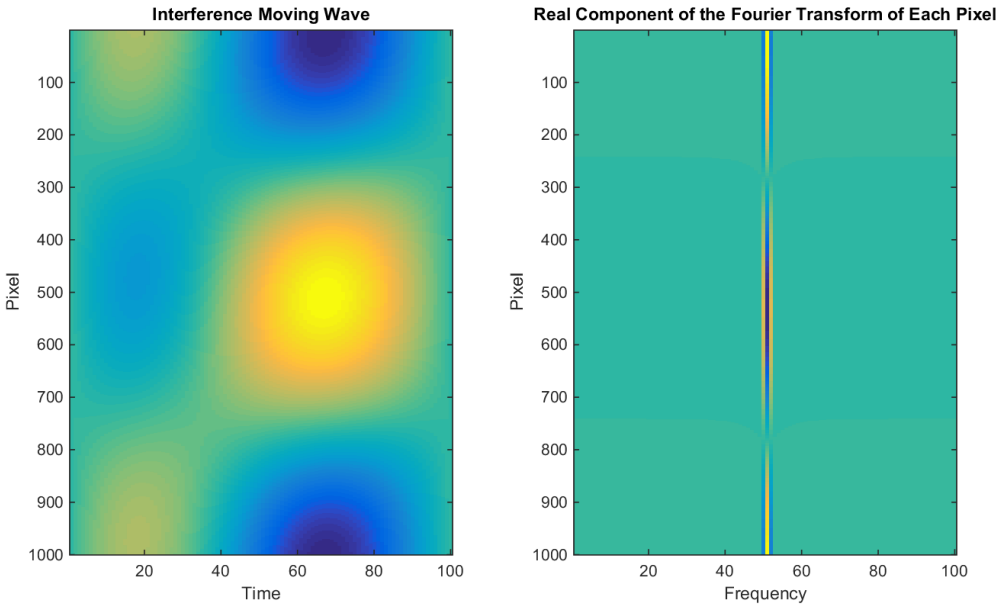

Figure 3-2: On the left, the displacement of a given column of pixels is mapped out as a set of waves with constructive and destructive interference. On the right is the resulting FFT with the signal still spiking around one cycle for the temporal frequency, and displaying the wavelength corresponding to the displacement. The signal ranges from 1 to -1.

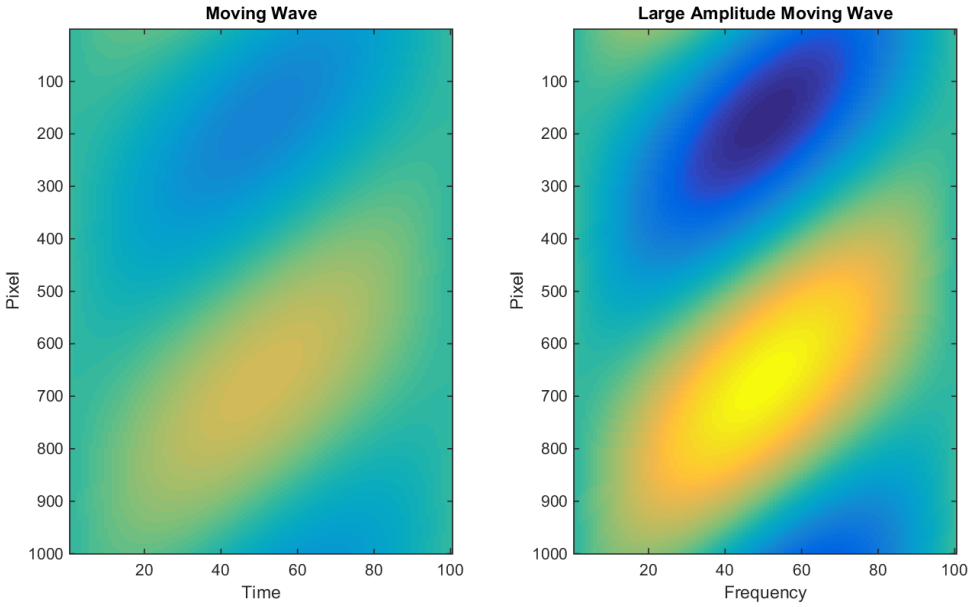

Figure 3-3: Two waves traveling across the surface. The left wave is half the amplitude of the second wave. Both images are shown with the same color scale demonstrating that a smaller amplitude wave displaces the background less. The wave travels one full period from the initial view beneath the wave in the 100 time steps.

waves so that the motion analysis can track the movement of the background. This is demonstrated in fig. 3-3 where the left signal is half the amplitude of the right.

3.2 Setting up and Taking Video

When setting up the experiment, the frame rate and the field of view restrict the velocity and size of the observable waves. These both need to be calibrated so that the observable velocity and wavelengths fit in the expected ranges for the fluids.

First the wavelength at which capillary effects start to dominate the dispersion relation is established by solving for what wavelengths start to be dominated by

capillary effects, when eq. (3.1) is true.

$$gk_0 \ll \frac{\sigma}{\rho}k_0^3 \tag{3.1}$$

This can be solved for for the varying expected surface tension to density ratios the fluid. For instance, the surface tension to density ratios for water between 0°C to 100°C varies between $0.7565 \times 10^{-4}\mathrm{m}^2\,\mathrm{s}^{-2}$ to $0.6147 \times 10^{-4}\mathrm{m}^2\,\mathrm{s}^{-2}$ because the surface tension varies between $75.64\mathrm{mN\,m}^{-1}$ to $58.85\mathrm{mN\,m}^{-1}$ while the density varies between $999.9\mathrm{kg\,m}^{-3}$ to $971.8\mathrm{kg\,m}^{-3}$.

By solving for when gravity and capillary effects are equal, an upper bound desired wavelength can be solved for as shown in appendix C.2. The result is shown by eq. (3.2).

$$\lambda = \frac{2\pi}{\sqrt{\frac{\rho}{\sigma}g}} \tag{3.2}$$

For the effect of the fluid properties to be much stronger than that of gravity, a constant factor imposing an order of magnitude difference can be introduced giving instead eq. (3.3)

$$\lambda = \frac{2\pi}{\sqrt{\frac{\rho}{\sigma}10g}} \tag{3.3}$$

For water, the resulting wavelengths that experience equal amounts of restoring forces due to gravity and capillary effects start around 0.0174m in cold water to 0.0157m in hot water, and the capillary effects start to dominate around wavelengths of 0.00552m to 0.00497m.

3.2.1 How to Choose the Field of View

The field of view (FOV) determines what size of wavelengths are visible. This needs to correspond to the wavelengths that are dominated by capillary effects. The field of view needs to both be large to have enough visible periods to estimate the wavelength and small to detect the small wavelengths associated with capillary waves.

For this, approximately six to ten periods were desired for accurate wavelength detection. Then the smallest wavelengths observable were limited by both the resolution of the camera's image sensor and the resolution of the dot pattern.

This can be determined by taking the largest wavelengths where capillary effects start to dominate from eq. (3.3), and then be multiplied by the minimum number of periods wanted to acquired the desired field of view. A range of six to ten periods gives a reasonable number to approximate a wavelength. This was approximated and validated by experiments when the field of view was too small. For somewhere in the range of six to ten periods, the field of view should be in the range of 3.3cm to 5.52cm.

From this calculation, the smallest wavelength visible can also be approximated given enough information about the resolution of the camera used. Using the same desired sampling rate of have at least six to ten pixels to approximate a wavelength,

$$\lambda_{min} = \text{FOV} \times \text{pixels per sample} \div \text{pixels} \tag{3.4}$$

3.2.2 How to Choose the Frame Rate

The frame rate determines the highest frequency of motion observable from the video. For the case of water, the angular frequency can be converted into frequencies giving the desired observable range for capillary waves.

By taking the observable range of wavelengths to be around 5.5cm or smaller, the capillary–gravity dispersion relation equation eq. (2.5) can be used to figure out what speeds the waves will propagate at. By manipulating eq. (2.5) to calculate the resulting frequency in hertz of the motion instead of the angular frequency, the calculation can be simplified to eq. (3.5).

$$f = \frac{1}{2\pi}\sqrt{gk_0 + \frac{\sigma}{\rho}k_0^3} \tag{3.5}$$

For the example wavelengths given in section 3.2, the dot pattern should experience at least six to ten full periods of motion at the slowest frequency to be used in analysis. Other factors to take into consideration when deciding a frame rate, include the amount of light available to get a well-exposed video, the memory buffer limitations, and the duration of the video. Both of these will affect how long it takes to process the videos, and the maximum resolution of the videos.

For the high-speed video used in these experiments, the resolution starts to decrease at frame rates greater than 5000fps and the camera can record 10918frames at the maximum resolution fo 1024×1024. It takes roughly 7 to 9h to process a spatially downsampled 10918frame video in the first step of the process. For this experiment, the memory could be partitioned into buffers of 2729frames.

By figuring out the duration of the video and the number of periods P wanted for analysis, the approximate desired frame rate can be determined based on the Nyquist rate and the number of periods of motion desiredeq. (3.6).

$$\text{fps} = \frac{\text{frames} \times f_{\max}}{\frac{1}{P}\text{frames}} \tag{3.6}$$

By taking the maximum number of periods expected in a field of view, the upper limit of the propagation speed of the waves can be determined. For practicality, a maximum number of around 20 periods with the downsampled resolution of 512×512 gives around 25pixels in each period. The corresponding frequency of this wavelength is then calculated using eq. (3.5) by taking the desired field of view to get the wavelength and then frequency. For this an approximate wavelength of .25mm with a field of view of 5.6cm gives a corresponding frequency of 176Hz. Then by using eq. (3.6) and using a minimum sampling of 6frames, the approximate frame rate can be calculated to 1056fps.

3.3 Extracting Motion Signal

Using a combination of the processes used in Phase-Based Video Motion Processing[37], Visual Microphone[15] the motion signal related to the dispersion equations, and therefore fluid properties, can be extracted. Like in [14], the motion signal is decomposed into individual frequencies to obtain a spectrum at each spatial pixel

First, the same technique described in [37] is used to extract the motion. In order for the motion of the fluid to be visible, there is the dot pattern placed beneath the bowl of the fluid similar to [39] as shown in later in fig. 4-1. This makes it so that the algorithm in the Motion Processing can track the relative movement of the dot pattern caused by waves instead of relying on tracking either difficult to track changes in a more uniform background or sparse specularities on the surface of the fluid.

The motion is extracted by using the differences between the phase coefficients in the complex-value image pyramids of the video. This local motion is encoded as a phase variation over the video which can be temporally processed by using a DC balanced filter to isolate individual sub-bands of frequencies in the motion [37]. In this space, the relative direction of the motion is encoded in the phase and it can be plotted by encoding the phase with hue and the magnitude of the motion with saturation as done in [14] and [15].

This process has been used to be able to extract the frequencies that a material vibrates at in Visual Vibrometry[14] and to analyze the specific shapes and frequencies of natural modes that rods and fabrics vibrate at. In addition, the Visual Microphone[15] paper was able to use this process to recover the source of vibrations in an object. Similarly, this project is using it to recover the relative speed of different wavelengths in a fluid.

3.3.1 Motion in Fluids

In fluids, the amount of refraction is determined by the refractive index and it determines how much the background is distorted by looking through the fluid. As a wave is propagating across the surface of a fluid, the wave acts like a lens and will bend the light based on the ratios of the refractive indexes between the mediums and the angle of entry or exit. The light will bend depending on the angle that it enters the fluid. When there are waves, the angle of the light changes based on the position the light is entering or exiting the waveform above. It will shift the background deforming it based on that shape. Like [39], the wave will move across the liquid creating the same deformation to the background shifted by the movement in the wave. By tracking the deformation in the background, the velocity of the wave can be extracted.

The fluid properties can then be calculated by using the speeds at which different wavelengths propagate through the fluid. In this case, as long as the fluid is refractive, we can use the code and techniques associated with this technique to extract the velocities at different frequencies corresponding to different wavelengths.

3.4 Match Filtering

To efficiently calculate the wavelength visible at a given frequency in the video, match filtering is performed on the space by using a set of circular wavelength match filters parameterized by the frequency of the expected wavelengths and the center of the circles. This is reasonable since the extracted motion for relative frequencies in the videos has a predictable concentric circle structure. This is most likely a result of constructive and destructive interference of waves propagating from the edges of the bowl containing the fluid. If each point along the ring of the bowl were to generate a specific wavelength, the resulting signal consists of concentric circles with the same

wavelength as explained later and shown in fig. 3-4.

The resulting match filter finds both the likely center of the concentric circles, and displays the maximum response for each spatial frequency at each temporal frequency. This creates a peak around the likely matches which can be used to fit to the dispersion equation. In the match filtering, the process assuming independent and identically distributed Gaussian white noise.

The equation used to generate each match filter basis is

$$B(x,y) = \exp^{2\pi i f\sqrt{(x-o_x)^2+(y-o_y)^2}-\Phi} \tag{3.7}$$

where B is the resulting basis function, ω is the frequency of the wave form, o_x and o_y are the origin of the wave, Φ is any phase shift, and x and y are the pixel location.

3.5 Estimating Surface Tension to Density Ratio through Fitting

After the match filtering is computed on each frame of the video, the results can be compiled into an image showing the strongest response for each wavelength for each frame. The strength of each wavelength and frequency pair should follow the dispersion relation.

The fitting can be done in two methods. One method assumes that the value for gravity in the results is correct at $9.81\mathrm{m\,s^{-2}}$ and fits for the surface tension to density ratio in the dispersion equation. The second method doesn't assume a value for gravity and fits for both gravity and the surface tension to density ratio.

In either case, the data is transformed into a space easier to perform the dispersion fit. The frequency analyzed in the video is converted into the angular frequency seen in the original dispersion equations. The corresponding wavelength counts seen in

each temporal frequency is then converted into the appropriate k_0 value dependent on the field of view. This makes it so that the results can be fit using and equation of the form

$$x^2 = 9.81y + my^3 \tag{3.8}$$

where x is the angular frequency, m is the slope from the surface tension to density ratio, and y is the corresponding wave number (k_0).

The fitting process starts by taking the energy map generated by the match filtering. From the match filtering and field of view calibration, the corresponding expected wave numbers k are calculated. To make the fit more robust to noise, first the data weighted by energy by raising it to the fourth power, and second a mask was applied to the data before fitting. As a note, good fits were still accomplished with smaller or no energy weighting done. The mask excludes anything outside a buffer of the observed signal and the erroneous temporal low frequency matches.

If the fitting is only the surface tension to density ratio,

3.6 Implementation Details

The wavelength matching method used needed to be robust to noisy motion signal, to be able to find small differences between wavelengths at each temporal frequency, and to be able to match to a wave pattern that doesn't have a known center point.

3.6.1 Concentric Circles

The match filter took the form of concentric circles because of observed motion. Since the fluid is contained in a bowl, the wave source can be thought of being generated at all points along the bowl's edge. I setup a simulation to justify this which can be seen with fig. 3-4 where waves starting from points around a circular bowl are progressively added using eq. (3.9). The simulated resulting pattern is concentric

circles.

$$B = \sin\left(2\pi(.1f)\sqrt{(x-o_x)^2+(y-o_y)^2}\right) \tag{3.9}$$

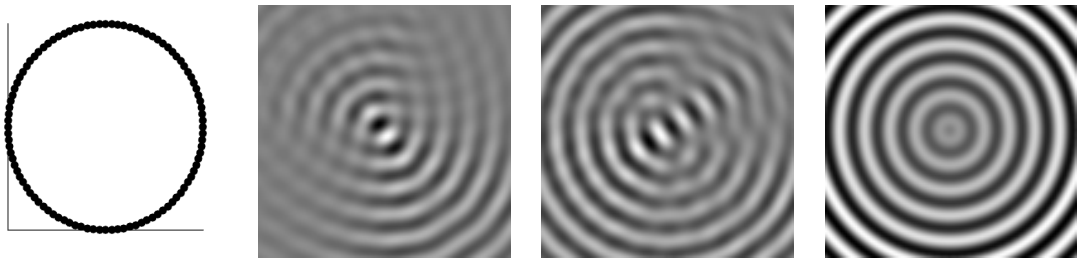

Figure 3-4: The resulting wave pattern after adding in multiple wave sources from around the ring of the bowl. Each image consists of adjacent waves progressively being added based on the origins in the first image.The resulting structure consists of concentric rings with 30 of 100 waves, 80 of 100 waves, and 100 of 100 waves around the bowl.

3.6.2 Match Filter Parameters

There were multiple decisions made when implementing the wave counting algorithm. Many were influenced by the fact that it's computationally expensive to perform numerous convolutions over a large number of high resolution images. The overall runtime of the matching process is dependent on the number of convolutions performed to find the likely wavelength by taking the maximum response over all possible shifts for each basis.

The main parameters of the match filter process consist of the range of wave numbers to be matched against, the size of the filter, and the resolution of the filter.

Once the parameters were chosen, the match filter could be run over the decomposed extracted frequency slices from the video. Each match filter would test the motion response for a given temporal frequency. Although phase of the motion often show a strong signal it is discontinuous. To avoid discontinuities in the phase images,

the match filter was tested against the real component of the motion signal.

3.6.3 Match Filtering Resolution

The match filter was tested with a high resolution (100 division per wave number) and increasing noise to test the accuracy of the matching. A sample of the respond and matched wave number are shown in fig. 3-5.

The corresponding response to the difference filters increases in the lower frequencies (larger wave numbers) as more noise is added fig. 3-6.

3.6.4 Match Filter and Noise

In the ideal case, the match filter is robust to a large signal to noise ratio where the noise is a Gaussian with $\sigma = 10$ and the input is range 1 to -1. Example responses are shown in fig. 3-7.

3.6.5 Basis Size for Match Filtering

When doing the wavelength matching in the videos, the centers for the concentric circles should align. Using the hypothesis that the concentric circles are generated by the container of the fluid the inner most ring will be in the center or near the center of the bowl. For this, the match filters generated should account for the possibility of the center of the concentric circles not being in the center of the video frame. The simplest way to do this was to create a match filter twice the size of the video frame. This allows for accurate matching even with the center of the circles being on the edge of the video. This works as long as the field of view of the video captures the center of the bowl.

If there is the possibility of the center of the rings being outside the field of view, then the basis for the match filter can be increase further in size to account for it.

Method	Runtime s
conv2(B,frame,'valid')	4936.694464
conv2(B,double(frame),'valid')	240.792090
conv2fft(B,frame,'valid')	1.820964
conv2fft(B,double(frame),'valid')	2.505533

Table 3.1: The two methods to perform a convolution consist of performing a convolution in the space domain or a multiplication in frequency domain. MATLAB's conv2 is the space domain convolution. The conv2ftt library implements a time domain convolution using FFT and multiplication in the frequency domain. B is the basis function or match filter at 2048×2048. The frame at 1024×1024 represents frequency slice extracted from the video. The 'valid' option is used to restrict the portion of the convolution result needed to the areas where the video frame completely overlaps with the basis.

3.6.6 Optimization

Since the match filtering needs to be done at many frequencies with a large complex valued image and the corresponding extracted motion information from the video, the process needs to be reasonably fast. The original implementation of the match filter took on the order of days to process 30frames of video after using MATLAB's built-in Run & Time to find the computational bottle-necks and optimize the runtime. The resulting methods and runtimes are list in table 3.1. All of the times were clocked on the same machine with a basis size of 2048×2048pixels and a frame size of 1024×1024pixels.

For small images, the runtimes for each method are comparable, but onces the images start getting large than 128×128 for the frame size, a 2D Fourier transform approach to convolution (conv2fft) runs faster than the spatial 2D convolution (conv2). conv2fft performs an fft on the input images to transform them into the frequency domain and then converts the resulting multiplication back into the space domain. The most likely reason for the threshold in performance between the two methods is that transforming the image into the frequency domain takes $n \log n$ time but once the images reach a certain size the convolution in the space domain is com-

putationally more expensive than converting into the frequency domain, performing a multiplication, and converting back to the time domain. This reduces the problem from $O(n^2)$ to $O(n \log n)$.

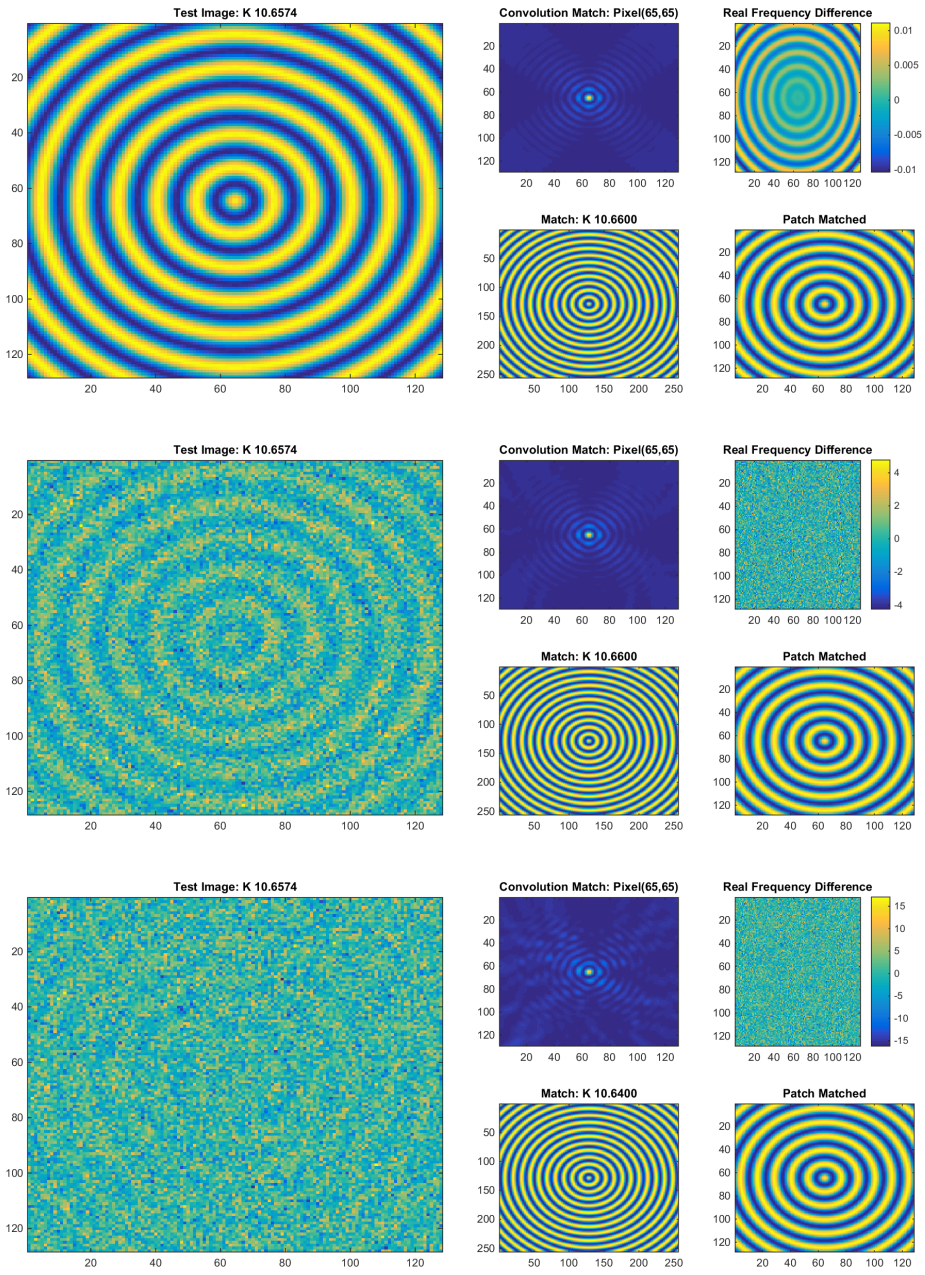

Figure 3-5: A non-discrete wave number tested with a resolution of 100 divisions per pixel. The original signal consists of a concentric circles with the wave number 10.6754 ranging from 1 to -1. The matched k is the value of the wave number of the filter with the strongest response. The smaller plots correspond to finding the center, the difference between the real signal and matched signal, the basis matched to, and the patch of the basis that was matched. The original signal is convolved with the larger basis to enable matching to a waveform without assuming the center of the circles to be the center of the field of view. The first row is the pure signal. The second row has added Gaussian noise with $\sigma = 1.25$, and third row is $\sigma = 4$.

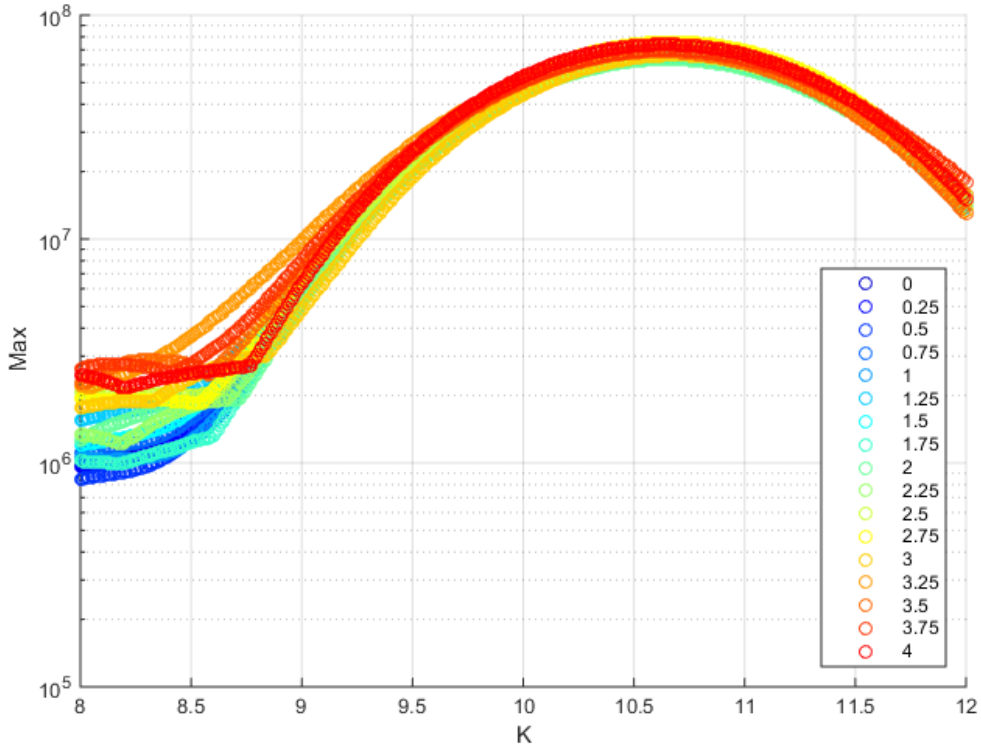

Figure 3-6: Each color corresponds to the match filter response of the combined signal from -1 to 1 and added Gaussian noise. Each value corresponds to the standard deviation of the added Gaussian noise. The increase in noise gives a stronger response in the lower frequencies. As the noise is increased, there is a slight, but small shift in the maximum response of the filter.

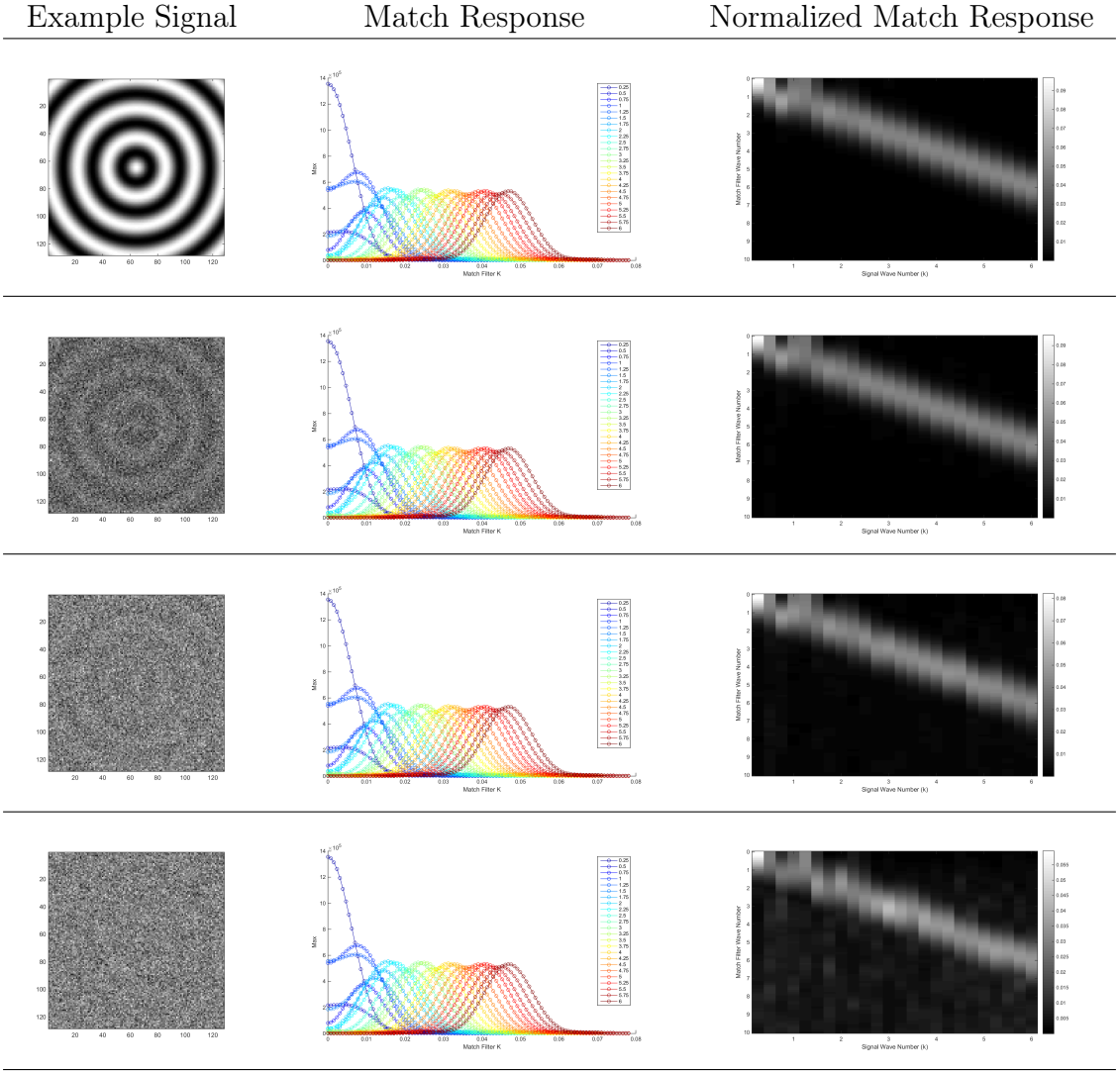

Figure 3-7: The match filter response for multiple low frequency wave numbers (indicated in the legend). The first column shows an example wave pattern going from a clean signal to an extremely noisy signal The second column shows the response for each wavelength (color) tested at the noise level and the response of the range of match filters tested. Each colored curve corresponds to the range of match filters tested and their response. The right column is a different visualization of the second column where the x axis corresponds to the wave number of the signal, the y axis is the wave number of the filter tested, and the intensity is the strength of the filter response. The first row is the pure signal range 1 to -1. The second row is the signal with noise $\sigma = 2.5$ the strength of the signal, third row is the signal with noise $\sigma = 5$, and fourth row is $\sigma = 10$.

Chapter 4

Experiments

Two experiments were performed to try to extract fluid properties from video. The first experiment consisted of recording high-speed videos varying the temperature of tap water. These could show that the surface tension to density ratio decreases as the temperature increases. The second experiment consisted of taking high-speed video of glycerol. This could show that glycerol has a lower surface tension to density ratio and the waves exhibit a damping effect due to the higher viscosity.

4.1 Setup

High-speed videos of fluids were collected by using a high-speed video camera (HSV) capable of a maximum 5000 frames per second(fps) at 1024×1024 resolution with a 90mm Macro lens. The Macro lens was chosen because it had the largest possible magnification value of the available lenses with a manual aperture ring. The minimum field of views for each lens is shown in appendix A.1.

The video collection took advantage of the high-speed video's partition option allowing four videos of 2729 frames at maximum resolution to be collected before having to empty the camera's buffer by saving.

The Photron SA-5 HSV was used with an approximate camera to subject distance (σ) of 42cm. The LED light, used to illuminate the bowl of liquid, had two optimal positions, one where it was placed directly beside the bowl with a slight downward angle, and the other using a stand and angled towards the bowl at the same height as the HSV. These two setups are shown in fig. 4-1 and fig. 4-2. The typical fluid height was around 5.5cm providing the sufficient depth to assume deep water waves. The videos were shot over the center of the 8" (20.3cm) bowl to be able to ignore boundary effects. Beneath the bowl was a dot pattern used to track sub-pixel motion [39]. The size of the dots was chosen experimentally, and multiple dot patterns are shown in fig. 4-3.

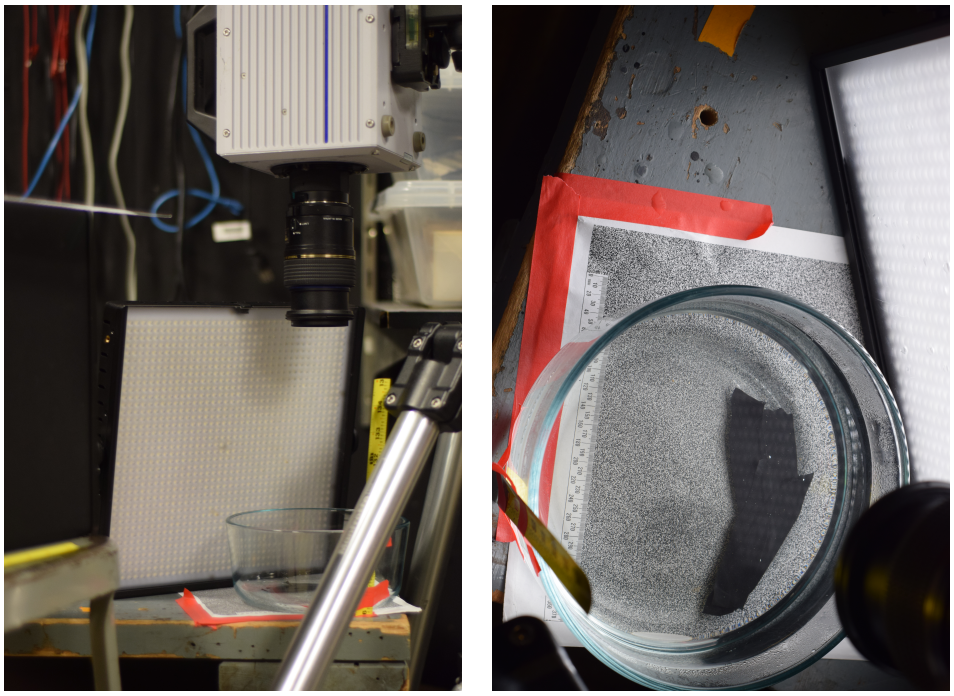

Figure 4-1: Setup when the light is next to the bowl.

To amplify the expected signal range, a ramp of 30Hz to 300Hz with $20,000$ samples and duration of 3s was played from a loud speaker as the video was recorded. The speaker was place on a stool away from the liquid's table to minimize vibrations

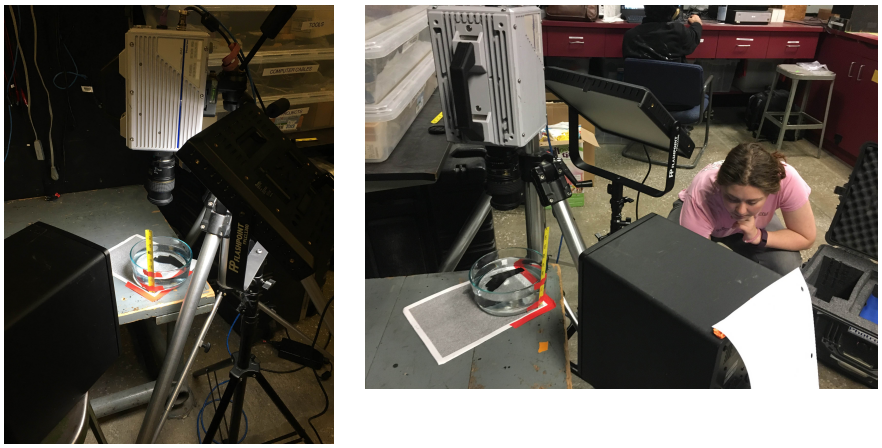

Figure 4-2: Setup when the light angle down pointing towards the bowl.

of the table.

4.1.1 Properly Measuring Field of View

Given the ideal thin lens equations [24], the field of view can be calculated given eq. (4.1), where w_i is the width of the image sensor, w_σ is the field of view, σ is the camera to subject distance, and f is the focal length of the lens. $\frac{w_i}{w_\sigma}$ is also more commonly known as the magnification or m.

$$\frac{w_i}{w_\sigma} = \frac{f}{\sigma - f} \tag{4.1}$$

This works when the focal length of the lens doesn't change. However, it is common in Macro lenses to experience "focus breathing." "Focus breathing" occurs when focus is achieved by changing the effective focal length of the lens hence altering both the field of view calculated and magnification [3].

Since the expected wavelengths are from surface waves, the field of view corresponding to the motion of the dot pattern is calculated by measuring the area visible from the perspective of the camera above the dot pattern. There are many ways to

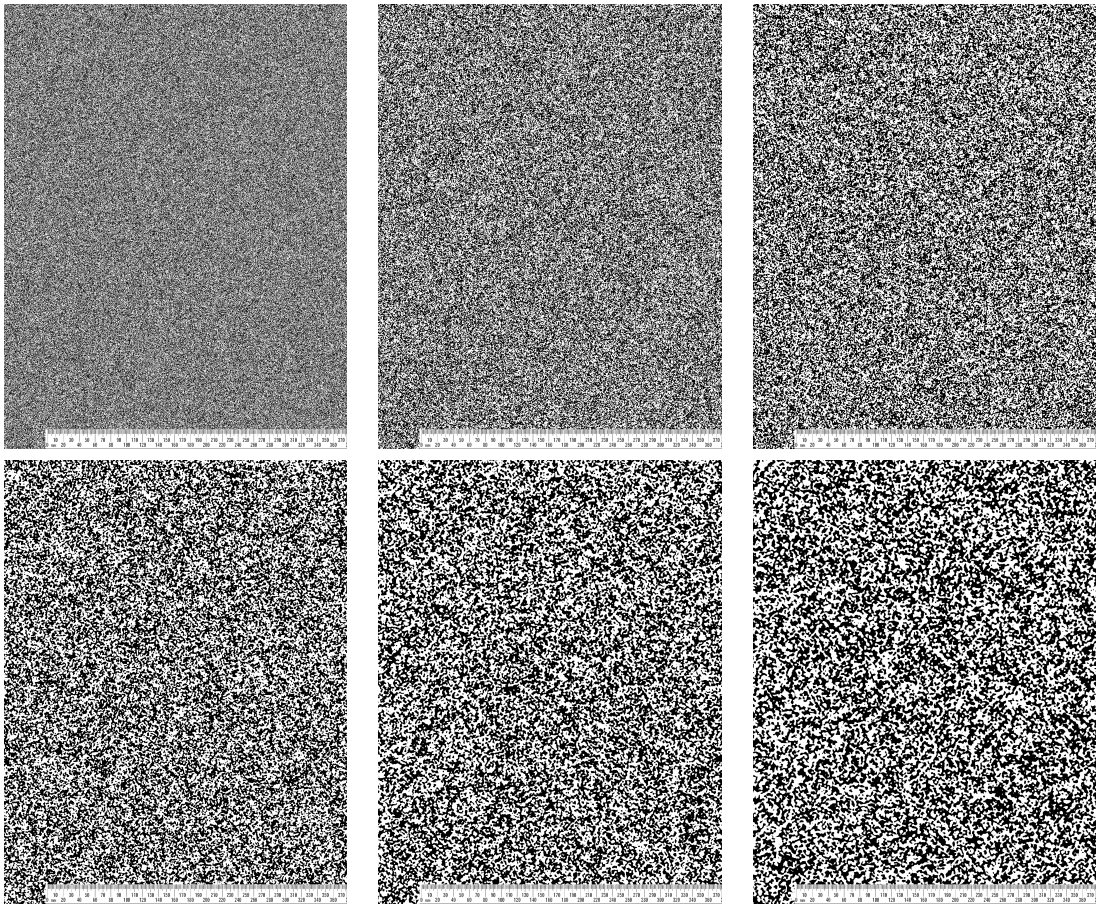

Figure 4-3: Various dot pattern sizes generated for a 8.5" $\times$ 11" piece of paper. The smallest dot pattern on the top left was the pattern used in the experiments in order to get a maximal motion resolution. Each dot pattern has a scale printed on the sheet for calibration.

try and calculate this measurement, covered later in section 5.5. The way decided on and used for the calculations consists of focusing sharply on the dot pattern using a shallow depth of field and then establishing a well-exposed image with a large depth of field capable of viewing both the dot pattern and the surface of the fluid in focus. This means the field of view from the perspective of the camera can be calculated without having to change the focus of the lens and circumvents the issues from focus breathing..

To accurately measure the field of view on the surface, there was a cut section of a tape measure that would float on the surface. An image of this tape measure section was taken to determine the field of view.

To show the differences between calculating the field of view from focusing on the dot pattern versus focusing on the surface of the fluid is shown in fig. 4-4.

FOV from Bottom

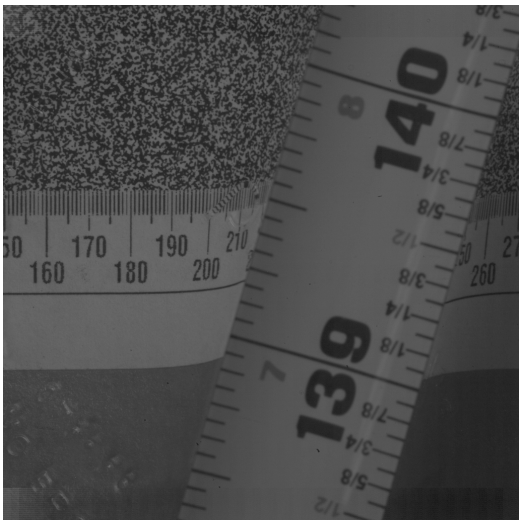

FOV from Surface

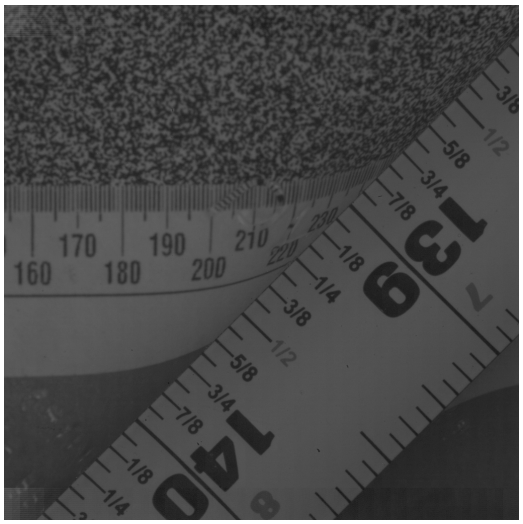

Figure 4-4: Field of view differences between sharply focusing on the dot pattern beneath the bowl and focusing sharply on the surface of the water. The field of view differences equate to 4.8cm versus 4.3cm. The larger field of view is focused on the bottom.

4.2 Temperature

The capillary effects of a fluid change based on temperature. Water is easy to acquire and heat, and has known values for surface tension and density at various temperatures [36]. This experiment also able to ignore the effects of viscosity because of water's low viscosity, $\eta = 8.94 \times 10^{-4}\mathrm{Pa\,s}$, $\nu = 1.004 \times 10^{-6}$ [1][26]. The table of values for water can be seen in appendix A.2.

4.2.1 Setup

Water was boiled and then poured into the Pyrex. All the HSV settings were preset at 1000fps, and had four partitions. In addition, the camera was pre-focused to the approximate water height so the highest temperature videos could immediately be collected. After the hottest temperature was recorded, the following videos were recorded at approximate 5°C temperature changes.

The temperature of the water was recorded using an infrared thermometer. Infrared thermometers assume that most surfaces have a high emissivity when calculating the corresponding temperature. With reflective surfaces, the thermometer may return a lower temperature if the surface is reflective. To correct for this, a black piece of non-reflective tape was placed at the bottom of the inside of the bowl to gather the temperatures.

4.2.2 Temperature Resolution Possible for Given Field of View and Properties

The experiments were setup with a field of view around 4.6cm. Using the known values for water in the dispersion equations and the number of periods visible in the field of view, the pixel difference for a given temperature change of 10°C and 5°C can be calculated, as shown in fig. 4-5.

4.2.3 Actual Temperature Resolution Measurable

Since it often takes some time to begin recording after preparing the boiling water, the range of reasonable temperatures to try and find a difference over is 70°C to 25°C was determined experimentally. This gives an expected change in the surface tension to density ratio demonstrated in fig. 4-6. The observable temperature differences will give around a 0.7pixel difference per wavelength for 5°C temperature differences in

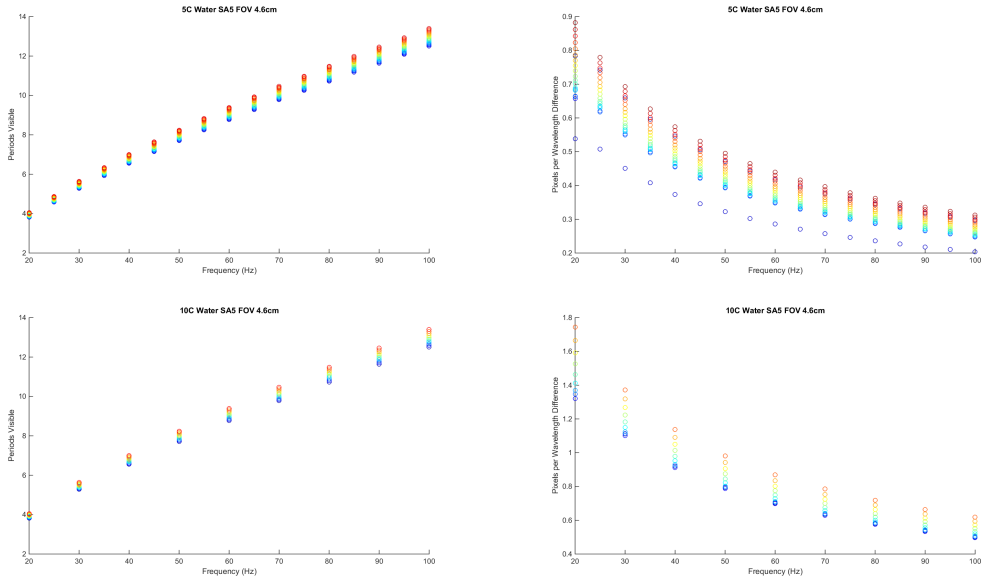

Figure 4-5: Expected pixel per wavelength differences in varying temperatures of water for temperature differences of 10°C and 5°C. All calculations done using the given sensor size of the SA-5 and with an measured field of view of 4.6cm over a temperature range of 0°C to 100°C and a resolution of 1024×1024 over the frequency range of 20Hz to 100Hz.

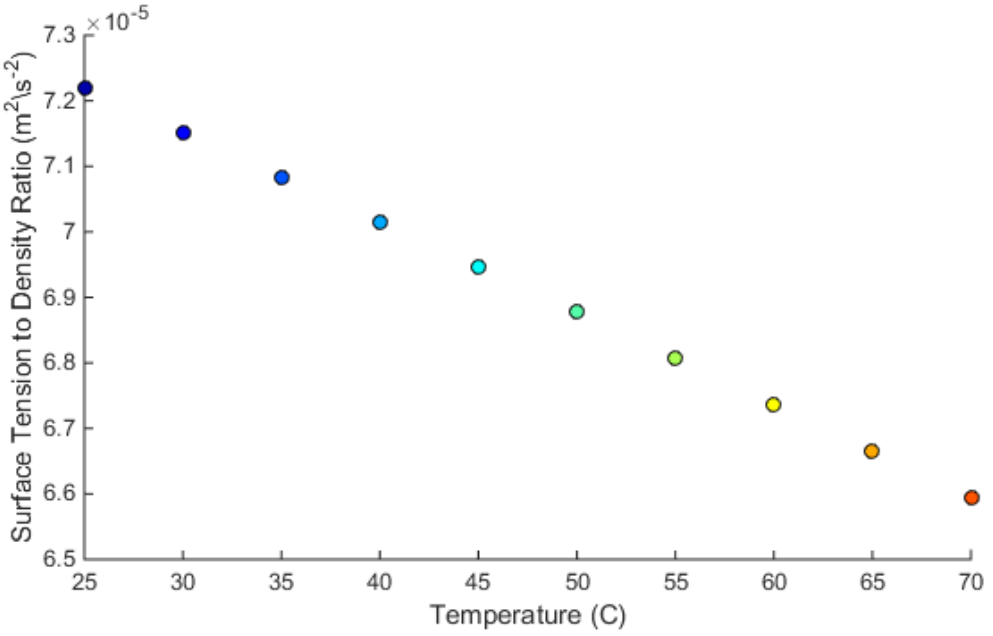

Figure 4-6: The expected variation in the surface tension to density ratios of water from 25°C to 70°C.

a 1024×1024 resolution and 1.4pixel difference per wavelength for a 10°C change. The corresponding pixel differences and periods visible for the temperature range of 25°C to 70°C are shown in fig. 4-8 and fig. 4-7 respectively.

4.2.4 Hypothesis

With an expected pixel difference of 0.7pixels to 0.3pixels using the given field of view per 5°C change, th experiments will have an overall temperature change of 35°C (70°C to 25°C). For the ten points collected (nine differences), there would be an expected difference of roughly 9×0.7pixel to 9×0.3pixel per wavelength visible for a resolution of 1024×1024pixel in the temperature range between slowest and fastest frequencies.

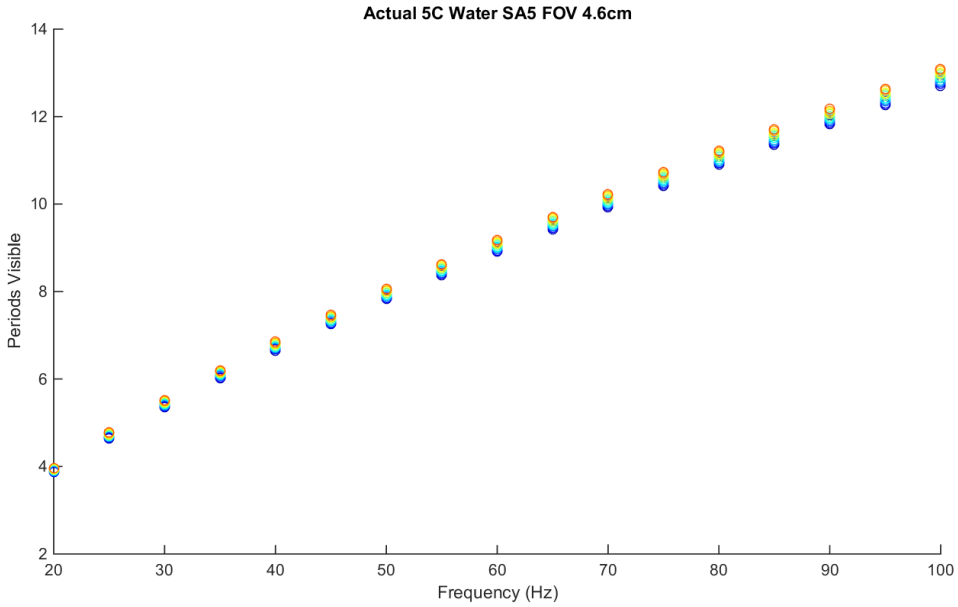

Figure 4-7: The expected number of periods visible for each water temperature at varying frequency slices. Temperature variation is from 25°C to 70°C.

4.3 Glycerol

For glycerol, the expected surface tension to density ratio is $\frac{.064}{1261}\mathrm{m}^2\,\mathrm{s}^{-2}$ ($5.0753 \times 10^{-5}\mathrm{m}^2\,\mathrm{s}^{-2}$) around room temperature (20°C to 25°C) . This is significantly different from water's surface tension to density ratio at room temperature of $\frac{.07275}{998.2}\mathrm{m}^2\,\mathrm{s}^{-2}$ ($7.2881 \times 10^{-5}\mathrm{m}^2\,\mathrm{s}^{-2}$). In the frequency range used in the temperature experiment (section 4.2), the glycerol wavelengths are still within a reasonable range. Additionally, solving eq. (3.3) for gives a maximum wavelength of .45cm but the capillary effects start to take over around 1.43cm eq. (3.2). These have corresponding frequencies of 14Hz to 62Hz. This overlaps enough with the water setup to suggest that the videos can be recorded with the same settings and also used for comparison.

The viscosity of glycerol, approximately 1.2Pa s at room temperature, will create a dampening effect on the waves.

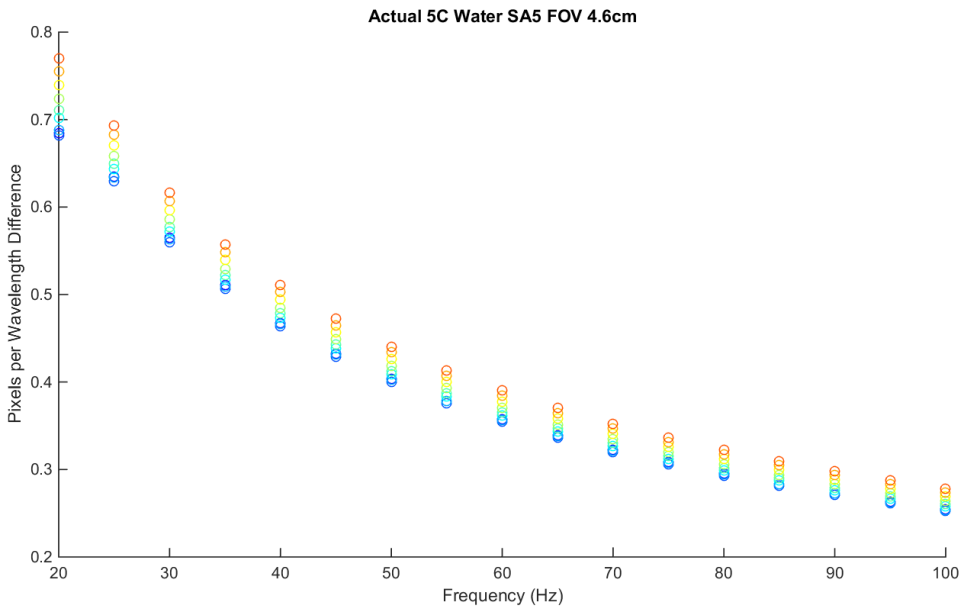

Figure 4-8: Expected pixel differences for a 5°C temperature change. The temperature varies from 25°C to 70°C

.

4.3.1 Setup

For these tests, first videos were taken of water around room temperature at 1000fps and 1024×1024 with the 30Hz to 300Hz ramp. At this time, the height of the water was noted on the side of the bowl to keep the depth of the fluids the same. The water was then removed and replaced with glycerol. The videos were taken similarly after refocusing on the dot pattern beneath the bowl. For completeness, the temperatures of both liquids were recorded.

4.3.2 Hypothesis

By using fig. 4-9, there is an estimated 0.25cm to 0.5cm difference between the expected wavelengths. Using a field of view of 4.5cm at 1024×1024, there should be approximately 56pixels of difference per wavelength in the glycerol and water wavelengths.

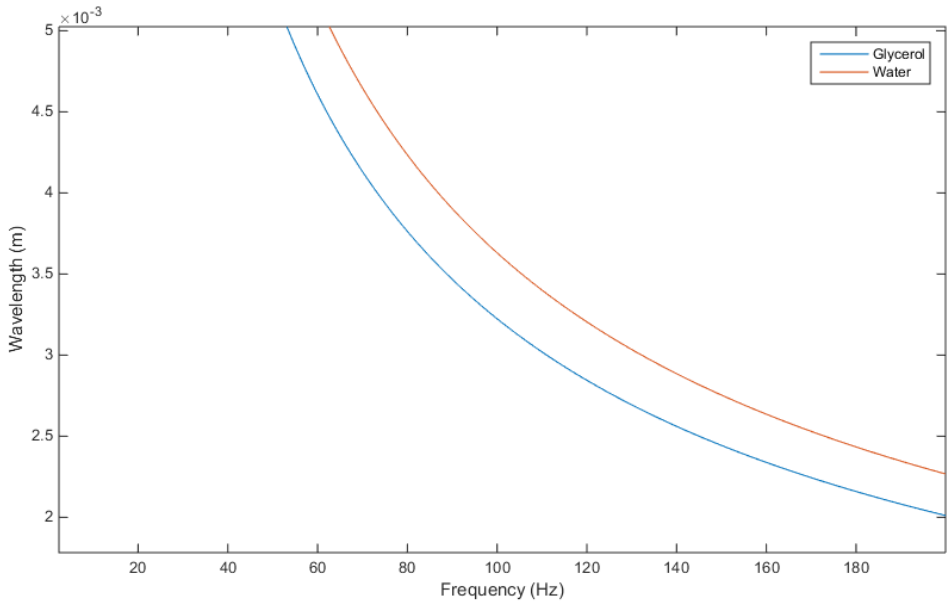

Figure 4-9: The two expected gravity–capillary wave dispersion curves for glycerol and water. Glycerol has a smaller surface tension to density ratio causing the waves to travel through the fluid faster than in water.

Chapter 5

Results and Discussion

In this chapter, the results from the experiments from chapter 4 are presented. Measurements were successfully extracted from the temperature experiments, and there was a strong trend of decreasing wavelength for higher velocity waves. However, ultimately, the results are currently inconclusive and require additional experiments for fluid analysis.

For the glycerol experiments, the glycerol had a large viscosity making it difficult to excite waves with a large enough amplitude in the smaller wavelengths. As the waves were excited in the fluid, the dampening by the viscosity made any motion from the waves negligible

Several additional experiments, calibrations, and methods were explored to try and figure out why the results deviated from theoretical values. These focused on verifying the field of view measurements, altering the experiment setup, and brainstorming causes for changes in the expected ratios.

5.1 Motion Analysis

The first step after each of the videos acquired was to extract the motion information. A wide spread of frequency slices that would be analyzed with the match filtering are shown in fig. 5-1. Note that the phase signal, though the strongest, has discontinuities because of the 0 to 2π range for angles.

5.2 Temperature

Recall from section 3.4, that in this proposed method, the velocity each wavelength is moving can be determined by matching filtering with a series of circular wave patterns. For each frequency of motion, corresponding to wave velocity, the wave origin and wavelength are searched for by using a series of match filters.

By taking the maximum response across all wave origin positions for each frequency and wavelength pair, the match filter returns an energy map that can be visualized as an image, indicating the areas of high energy. An example of a normalized energy map, displayed as an image, is shown in fig. 5-2. The normalization was done to account for amplitude changes since some wavelengths produced a stronger signal than others. This is most likely due to the bowl or water resonating around specific frequencies.

By assuming that the equation fitted should be the dispersion relation with minimal effects from viscosity, a line can be fit to the curve.

$$\omega^2 = gk_0 + \frac{\sigma}{\rho}k_0^3 \tag{5.1}$$

Since there are some sections of the video that had a stronger signal in the lower frequencies because of minimal signal at the expected frequency, the fitted data was masked as shown in fig. 5-3.

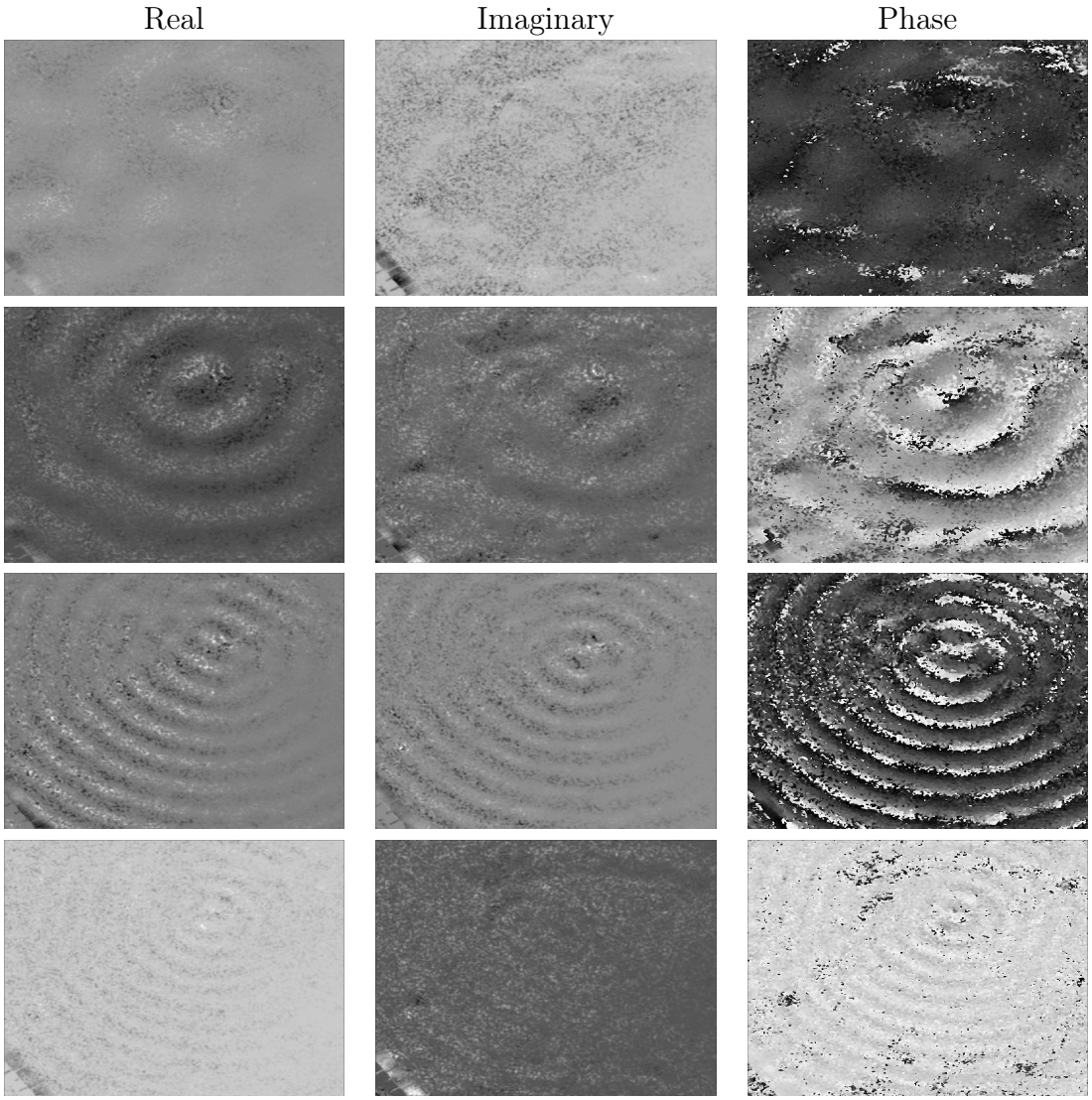

Figure 5-1: The frequency slices at 20Hz, 30Hz, 60Hz and 100Hz with their respective real, imaginary, and phase. Notice there are discontinuities in the phase resulting from the 0 to 2π boundary.

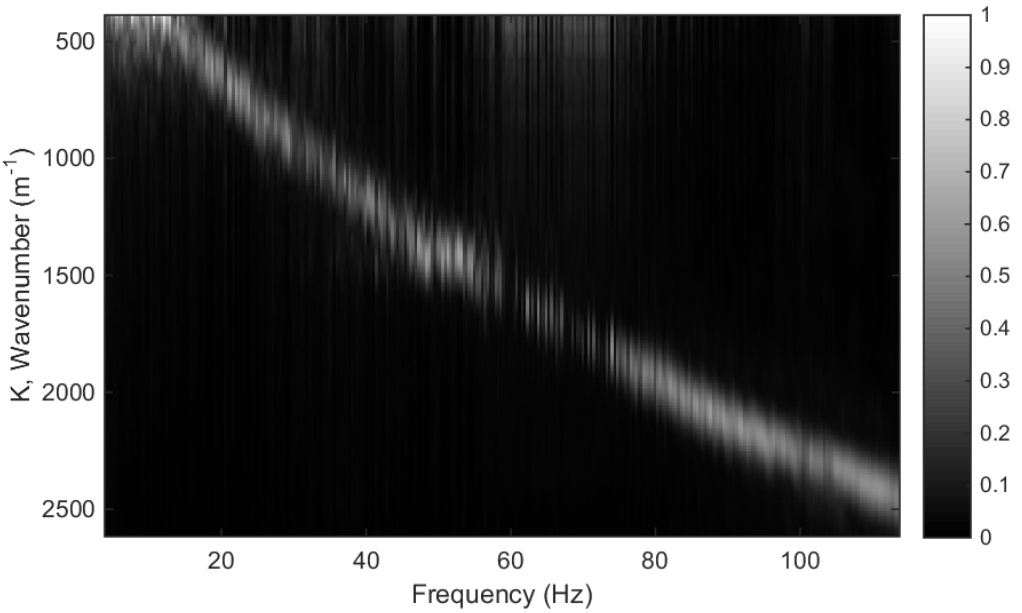

Figure 5-2: Normalized energy response resulting from matching filtering using the real portion of the motion information of the dot pattern.

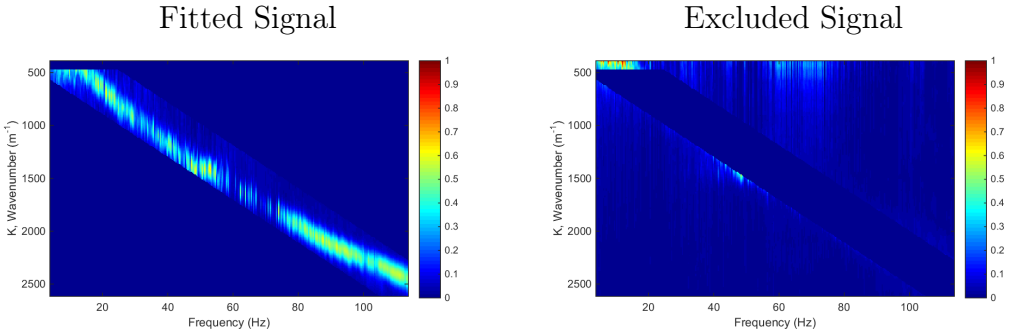

Figure 5-3: On the left is the masked data used when fitting to exclude the low frequency responses. It was generated to mask out areas with minimal expected signal. On the right, is the data excluded by the mask.

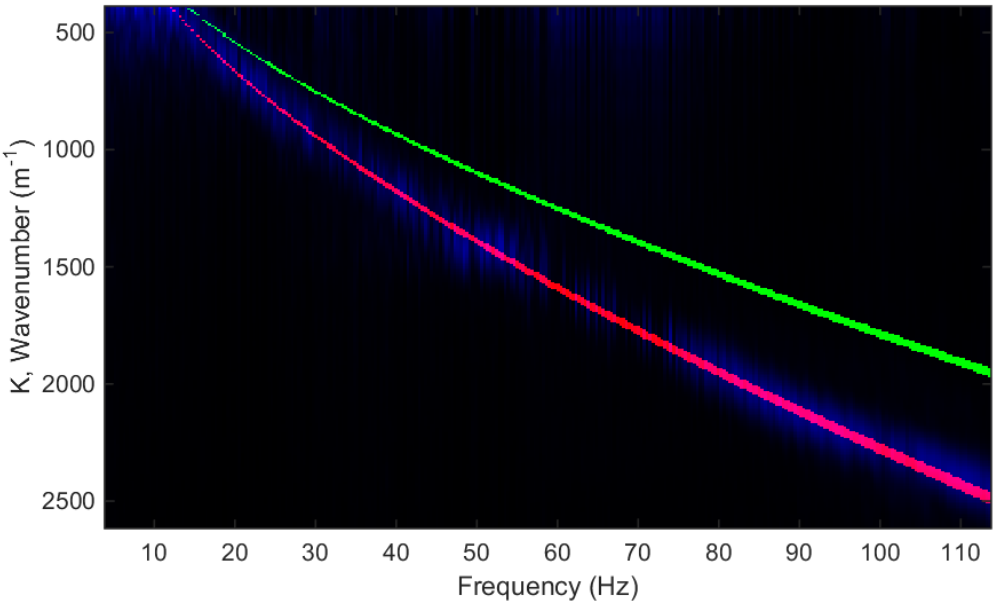

Figure 5-4: The resulting fitted curved drawn in red assuming that gravity is $9.81\mathrm{m\,s^{-2}}$ versus the expected line in green. The lines are thick because they were computed by using a threshold between the value at each frequency slice and the equation values. Pixels with a close enough value create the line.

After using the mask to take out unwanted bias towards the lower frequencies, the dispersion relation curve can be fit by either assuming gravity to be the proper value of $9.81\mathrm{m\,s^{-2}}$ or only assuming the general shape of the curve. Unlike in [4], the fits were done to eq. (5.1), instead of eq. (5.2).

$$\frac{\omega^2}{k_0} = g + \frac{\sigma}{\rho} k_0^2 \tag{5.2}$$

This process was then repeated for all the videos taken with the given setup. For the temperature experiments, this is nine videos over the temperature range of 68°C to 28°C.

The resulting fitted slopes assuming gravity as $9.81\mathrm{m\,s^{-1}}$ are plotted and fit in fig. 5-5. The fitted slope of the line is -0.0003×10^{-4} and the intercept is $0.3383 \times$

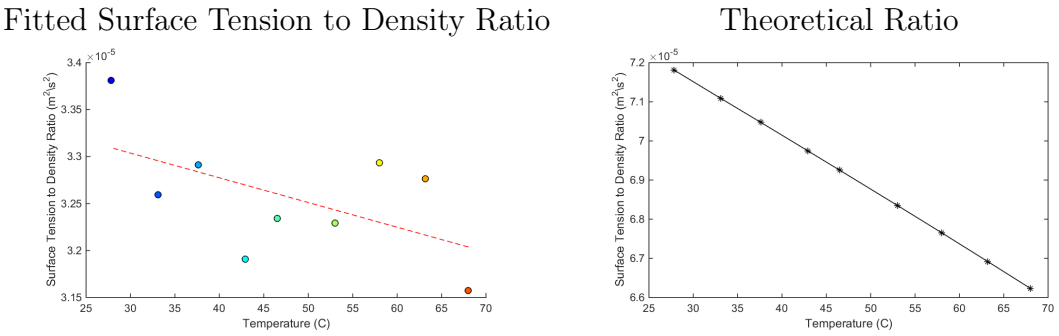

Figure 5-5: The resulting slopes fit when assuming gravity to be $9.81\mathrm{m\,s^{-2}}$ with a high resolution match filtering with sixteen division per wavenumber. The field of view used to calculate the wavenumber k is 4.8cm. The fitted slope of the line is -0.0003×10^{-4} and the intercept is 0.3383×10^{4} where as the expected slope and intercept computed from theoretical values are -0.0014×10^{-4} and 0.7569×10^{-4} respectively. The fit has an R^2 value of 0.3114

10^4, and the expected slope and intercept are -0.0014×10^{-4} and 0.7569×10^{-4} respectively. The slope fit had an R^2 value of 0.3114. For reference, the expected values and results can be seen in table 5.1.

The fits were also tested without assuming gravity. The results for fitting the value of gravity and the value of $\frac{\sigma}{\rho}$ are shown in fig. 5-7. The fitting excluded the 68°C outlier. This produced a fit slope and intercept for $\frac{\sigma}{\rho}$ of -0.0002×10^{-4} and 0.3274×10^{-4} respectively while the fitted value of gravity is 13.6776. The surface tension to density fit had an R^2 value of 0.5460.

The table of the fitted results for surface tension and gravity, and surface tension for each of the nine videos is listed for comparison in table 5.1.

5.3 Excitation of Waves

It was questionable if the waves needed to be excited by a speaker in order to have large enough amplitude to be picked up by the camera. To test this videos were collected with and without using a speaker. A result without using a speaker with

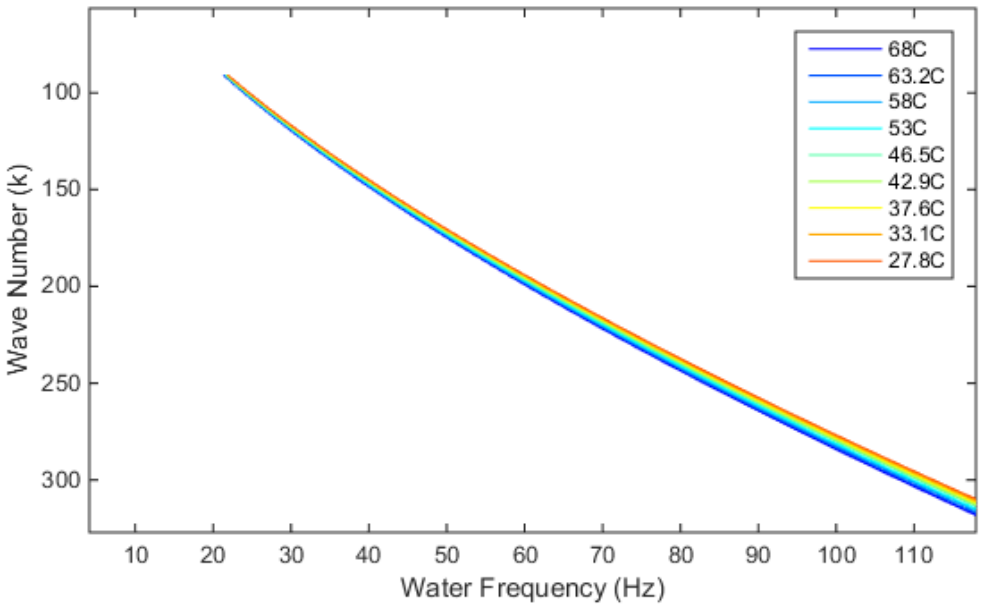

Figure 5-6: The theoretical curves for the dispersion relation of water using the experimental temperatures. The warmer temperatures are expected to have a higher wave number than the colder temperatures for a given frequency.

	Theoretical	Only Fitting $\frac{\sigma}{\rho}$	Fitting g and $\frac{\sigma}{\rho}$	
Temperature	$\frac{\sigma}{\rho}$	$\frac{\sigma}{\rho}$	$\frac{\sigma}{\rho}$	g
68°C	0.7182×10^{-4}	0.3157×10^{-4}	0.3250×10^{-4}	7.8397
63.2°C	0.7109×10^{-4}	0.3276×10^{-4}	0.3138×10^{-4}	14.9216
58°C	0.7048×10^{-4}	0.3293×10^{-4}	0.3201×10^{-4}	13.1985
53°C	0.6975×10^{-4}	0.3229×10^{-4}	0.3166×10^{-4}	14.1519
46°C	0.6925×10^{-4}	0.3234×10^{-4}	0.3163×10^{-4}	14.1634
42.9°C	0.6835×10^{-4}	0.3191×10^{-4}	0.3159×10^{-4}	14.2625
37.6°C	0.6765×10^{-4}	0.3291×10^{-4}	0.3210×10^{-4}	12.8887
33.1°C	0.6692×10^{-4}	0.3259×10^{-4}	0.3221×10^{-4}	12.2471
27.8°C	0.6623×10^{-4}	0.3381×10^{-4}	0.3226×10^{-4}	13.5871

Table 5.1: The numerical results from the two fitting types. Both the the fits have a slight trend of decreasing the surface tension to density ratio as the temperature increases as expected by the theoretical values.

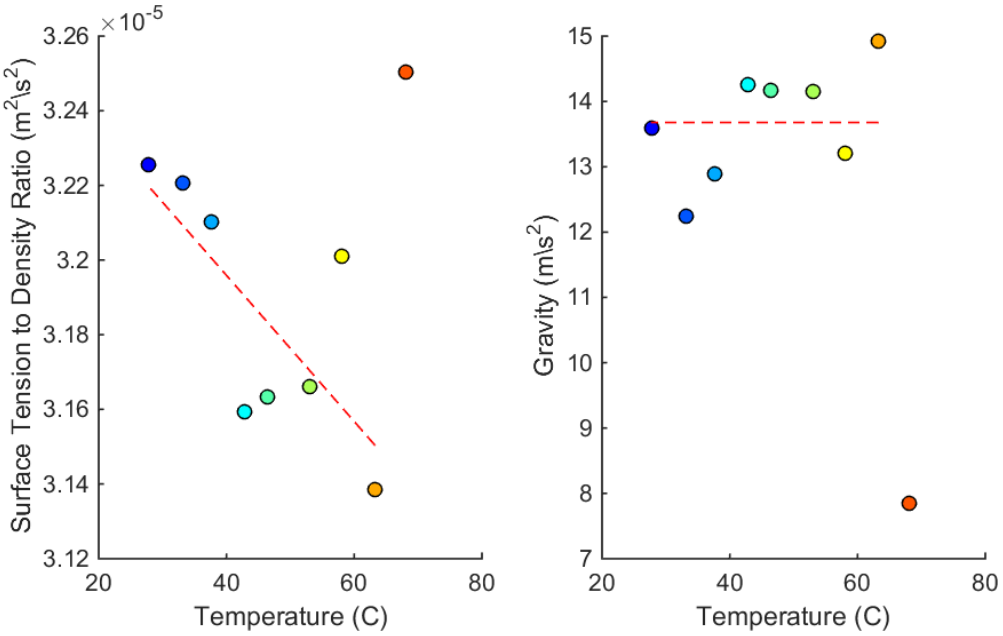

Figure 5-7: The results of fitting gravity and the surface tension to density ratio excluding the 68°C outlier. The fit of the slope and intercept of $\frac{\sigma}{\rho}$ is -0.0002×10^{-4} and 0.3274×10^{-4} respectively while the fitted value of gravity is 13.6776. The surface tension to density fit has an R^2 value of 0.5460

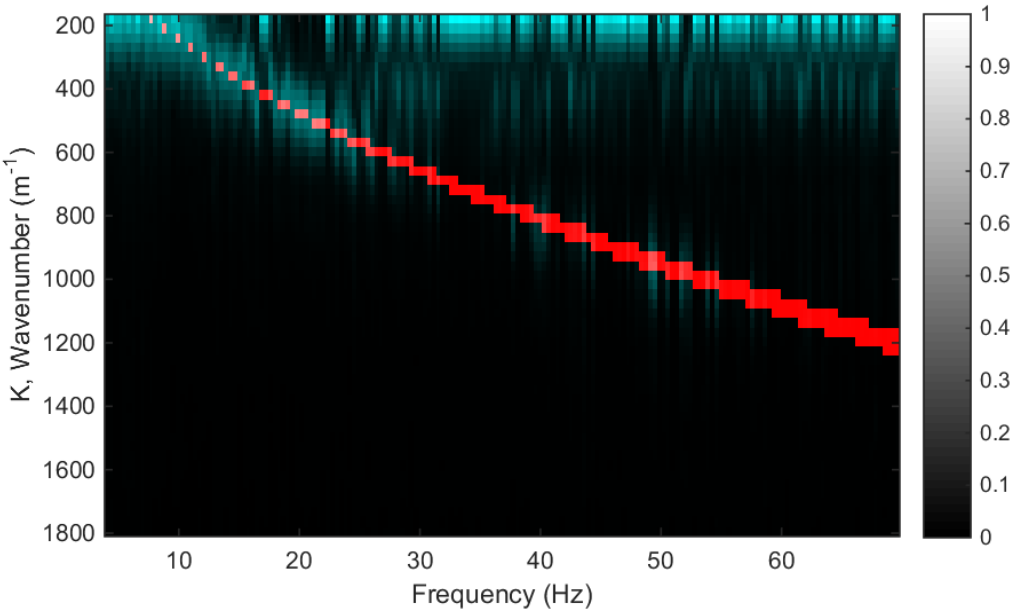

Figure 5-8: Normalized energy response in a small field of view around 3.3cm without a speaker strengthening the signal in the fluid. The line through the center of the plot denotes calculated fit line. The strong response to the lower wave numbers made it difficult to mask and calculate the fit line because the expected frequencies were a smaller amplitude.

a field of view around 3cm is shown by fig. 5-8. The results indicated that with a small field of view and no speaker, the signal was present but non-optimal.

5.4 Glycerol

Glycerol has an extremely high attenuation rate making it difficult to excite and observe capillary waves of reasonable amplitude [4]. From the videos taken of glycerol, the wavelengths observed were in the gravity range (larger than 0.45cm to 1.43cm) fig. 5-9. Once the temporal frequencies are high enough, the waves are influenced by viscosity which dampens the amplitude of the waves. This caused the videos collected to show gravity waves in the glycerol, but the capillary wave signal was too

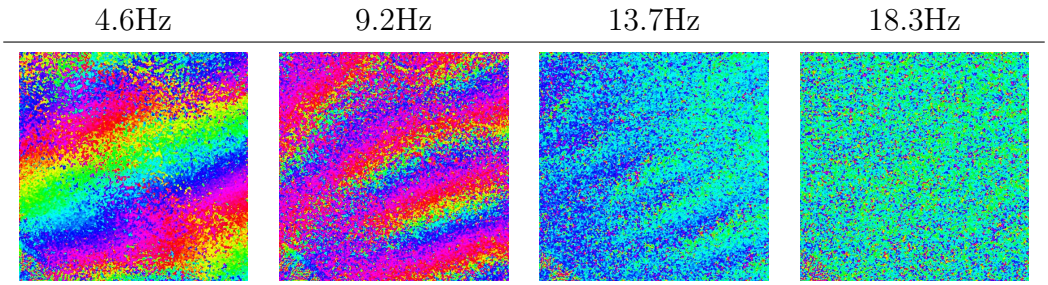

Figure 5-9: Four frequencies where the motion was analyzed from a glycerol video. The field of view is around 8cm making all of the observed wavelengths gravity waves. Additionally, the temporal frequencies for these wavelengths are theoretically too slow for glycerol's waves to experience capillary effects. The colors in these images use an HSV (hue, saturation, value) colormap to avoid discontinuities, and correspond to the phase of the motion at each pixel.

small.

5.5 Troubleshooting

The results from the wavelength fitting and spectral analysis produced fitted ratios for surface tension to density in water of about half the expected value (an average 0.6906×10^{-4} versus 0.3257×10^{-4}). In addition, the spectral videos for glycerol didn't produce visible waves to use in calculating the fluid property ratios.

5.5.1 Glycerol

Because [4] stated the difficulties of trying to excite small wavelengths in glycerol and the test videos had minimal success in observing motion in glycerol, the final videos for glycerol were taken in three different conditions. First the glycerol was in the same setup as the water with the speaker close but not directly contacting anything the bowl was touching. Second, the speaker's stool was pushed close to the table holding the bowl of glycerol so that the two were barely touching. Third, the

speaker was place directly beside the bowl of glycerol.

5.5.2 Water

Some possible sources of error where the expected values can deviate from the theoretical values consist of imperfections in how the experiment was conducted and the purity of the fluids. First surface tension decreases can be caused by impurities in the fluid. Tap water has a lower surface tension than pure water. This may account for a slightly lower surface tension to density ratio, but not the factor of two that is being observed. Second, the experiment was conducted in an open room that could have introduced dust particulates into the water surface also causing a decrease in the surface tension.

5.5.3 K Wave Number

Gravity

Since the fit value for gravity was near $13.6\mathrm{m\,s^{-2}}$ instead of the expected $9.81\mathrm{m\,s^{-2}}$, the way the k measurements were calibrated was checked and tested multiple times. However, the fit value for gravity may not necessarily be reliable since the portion of the dispersion relation being observed is dominated by the $\frac{\sigma}{\rho}k_0^3$ term at large k_0 values.

Field of View

The wave number is reliant on acquiring an accurate field of view measurement. A change in the field of view from 4.8cm to 6.1cm changes the current fit values to the expected values. As such, several methods were tested to find an accurate field of view measurement.

Since the distortion to the dot pattern is due to surface waves, the field of view

measurement needed to calculate the correct wave number should be the surface area of the top of the liquid visible from the viewpoint of the camera. Note that this depends on the type of lens used in the experiment. If a wide angle or short focal length lens were used in the measurements, at the same magnification the wide angle lens would have a larger difference between the viewed area of the dot pattern background and the fluid surface closer to the lens. In general, lenses with a focal length shorter than 35mm are consider wide angle while lenses with a focal length longer than 85mm are considered telephoto. Since the experiments use a 90mm lens, the amount of change in viewable background should vary less based on distance. This means that the area on the fluid's surface visible from the perspective of the camera won't be the same as the area of the waves directly above the dot pattern.

To calculate the field of view of the surface area, the first method of correction used the thin lens equations eq. (4.1). It was done by correcting for the effects from parallax, a change in the distance from the subject to the camera. Logically, this equation depends on the focal length of the lens. To perform the correction, the field of view at the distance of the dot pattern on the table was calculated by using a scale. This gave the effective distance of the table to the camera. Once the effective distance was calculated, then the change in distance from the table to the surface of the fluid could be used to move the camera to subject distance from table to the fluid surface eq. (5.3). Note that because of refraction, the effective distance from the camera to the dot pattern through the water is different than the distance from the camera to the table. The derivation can be seen in appendix C.3. Since the distance values in the calculations are small, a small difference in the camera to subject distance could create a large change in k.

$$w_{\sigma_T} = w_{\sigma_B} - \frac{w_i w_H}{f} \tag{5.3}$$

In this equation, w_{σ_T} is the field of view at surface of the water. w_{σ_B} is the field of

view at the bottom of the bowl (surface of the table). w_i is the width of the image sensor. w_H is the water height. f is the focal length of the lens.

This method of correction was verified experimentally by adjusting the camera to subject distance and taking field of view measurements as shown in fig. 5-10 where the points are recorded field of views and distances. The original distances and corresponding field of views fit the correct slope of a 90mm lens, however there is an offset in the recorded camera to subject distance. This is because the center point of the lens for calculations could be anywhere inside the lens. This shows the uncertainty associated with relying on absolute camera to subject distances.

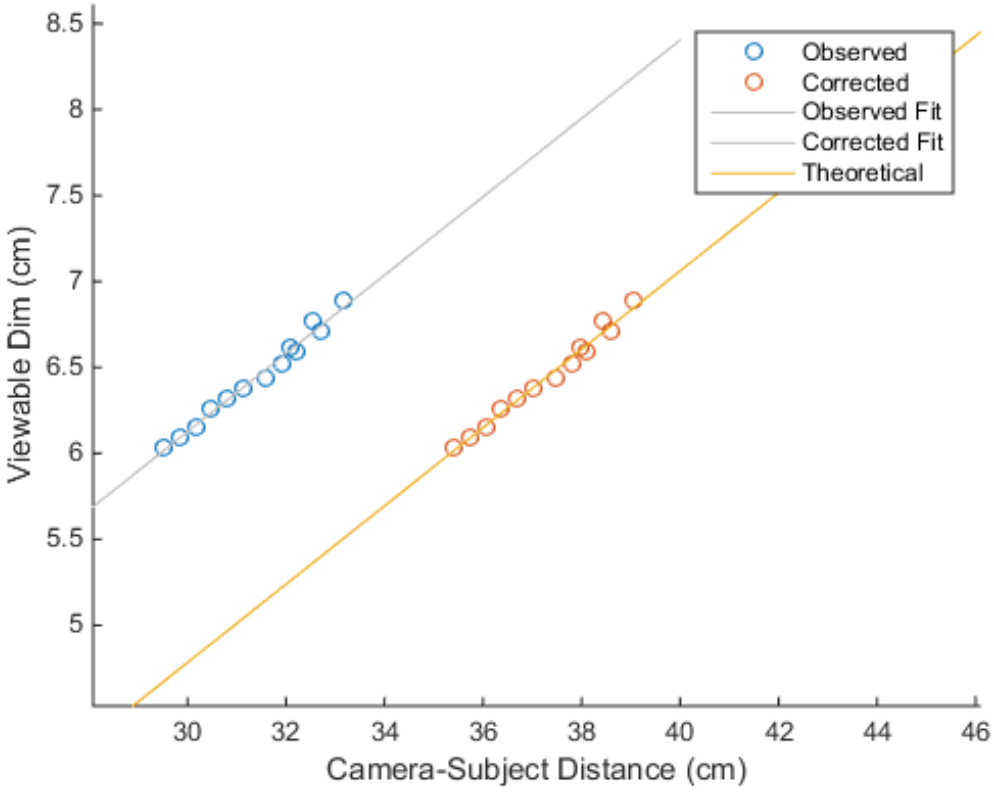

Figure 5-10: Calibration for field of view done fitting to the 90mm lens using the thin lens equations. The two lines show the importance of getting the effective camera to subject distance versus trying to measure the camera to subject distance.

Since this method required measuring the height of the fluid, another alternate method was tested to try and eliminate potential for error. The newer method consisted of focusing on the surface of the fluid with a chopped section of a tape measure for scale. This was a good idea in principal, but is dependent on ideal lens behavior which is unrealistic at small working distances.

Using lens equations works if the lens obeys assumptions associated with an ideal lens. Mainly, the lens can't change its focal length. However, it's common in Macro lenses to experience a phenomenon called focus breathing. This is when the lens changes its focal length to focus at a specific distance. Since the distances from the surface of the water to the camera are extremely close, it would be reasonable to expect the lens to exhibit some focus breathing. As such, the method for the measuring the field of view was changed again to further try to eliminate potential for error.

The final method using the depth of field describe in section 4.1.1 should be the most reliable of the three methods because it doesn't rely on taking measurements of the setup, and only relies on calculating the field of the view from the recorded images.

The fitted $\frac{\sigma}{\rho}$ ratios change from around 3.3×10^{-5} to 2.3×10^{-5} with this .5cm difference in field of view.

5.5.4 Observing Phase Velocity versus Group Velocity

Another source of potential error is what is being extracted using the motion analysis. Dispersion has two velocities that can be observed with waves in a fluid. One is the group velocity v_g the other is the phase velocity v_p. The group velocity is the change in ω relative to the change in k or $\frac{\partial \omega}{\partial k}$.

The group velocity is generally what is observed by the naked eye as the combination of all the individual wave packets traveling together and causing constructive

and destructive interference. There was some questioning as to the observed values being the group velocity since in practice a infinitely small subband for Fourier decomposition is impossible to achieve. This would suggest that the response would incorporate a group velocity (eq. (5.4)) with the phase velocity.

If the limits are taken as the k gets to extremely large or small values, the ratio between the group velocity and the phase velocity approach $\frac{1}{2}$ and $\frac{3}{2}$ respectively. This would have corrected for the factor of two if the waves observed were gravity waves. However, for large values of k the group velocity observed is faster than the phase velocity meaning that the observed k values at the lower frequencies would need to be even larger.

$$v_g = \frac{\partial \omega}{\partial k} = \frac{3\frac{\sigma}{\rho}k^2 + g}{2\sqrt{\frac{\sigma}{\rho}k^3 + gk}} \tag{5.4}$$

The most likely interpretation is that the Fourier transform done on the motion of the dots has both signal from the phase velocity and the group velocity with the strongest signal being the phase velocity.

Chapter 6

Conclusion

The goal of this project was to calculate and to observe fluid properties (surface tension, density, and viscosity) change through high-speed video analysis. This was done by two main experiments. The first experiment consisted of changing the temperature of water. The second experiment consisted of observing glycerol to compare to water. The motion in the videos was then decomposed by frequency. This resulting motion was match filtered to find the wavelength present at each frequency producing an energy map which could then be fit to the dispersion equations.

The resulting energy maps were fitted for values of the surface tension to density ratio assuming gravity, and were fitted for values of surface tension to density when not assuming a gravity of $9.81\mathrm{m\,s^{-2}}$. The fitted surface tension to density ratios did exhibit the expected inverse relationship to temperature. However, the observed ratios were off by a factor of two from the theoretical values, and the reasonings for this are still trying to be understood.

Overall, the current setup and uncertainty in the fidelity of the wave number measurements makes it difficult to extract information. There is a strong general trend in the slope of the surface tension to density ratio as the hotter temperatures have a smaller slope than the colder temperatures because the surface tension of

water decreases faster than the density. To further nail down possible errors in measurements, there are several additional experiments and setups that could be tried to debug why the values off by roughly a factor of two.

Possible experiments or alternate setups include performing the measurements with a shallower fluid. This would eliminate any ambiguity between measuring the field of view of the camera by diminishing the differences between the field of view of the dot pattern with the observed motion and the surface of the fluid.

Additionally, more liquids could be tested. The current fluids, pure glycerol and tap water, could be mixed providing fluids with varied viscosity. This would give more opportunities, other than pure glycerol experiments, to measure the dampening effect viscosity has on capillary waves. Also, any fluids with more noticeable differences in surface tension and density could be tested. For instance, fluid mixtures containing acetic acid (with a surface tension of $27.60\mathrm{mN\,m}$ and density of $1050\mathrm{kg\,m^{-3}}$) and water could provide a wider range of surface tension to density ratios. However, this could also be more difficult since the smaller the surface tension to density ratio, the smaller the wavelengths that need to be observed.

In addition to the current method, a more traditional machine learning approach could be used by breaking down the motion of waves at different frequencies for many fluids into sub-bands and training a model using known data. After training, the model could be used to perform predictions on unknown fluids.

Another extension of the project could be to use more opaque liquids and focus on the surface of the fluid. Here the motion of the surface specularities could be related to dispersion as only the motion at specularities would be observed instead of dot pattern. This may be more difficult because the motion information would be sparse. However there would be fewer uncertainties in the measurements due to directly observing motion on the surface of the fluid.

Appendix A

Tables

A.1 Lenses

Focal Length (f)	Minimum Working Distance (σ)	Max Magnification
28 mm	0.85 m	0.0341
50 mm	0.45 m	0.125
90 mm	0.25 m	0.5625
105 mm	0.21 m	1
200 mm	1 m	0.25

Table A.1: The minimum working distances, maximum magnification, and focal length of the lenses available. The 90mm lens was chosen because it had the highest potential magnification with a manual aperture ring. The 105mm has a larger possible magnification, but the HSV doesn't have the capability to drive an aperture ring making.

A.2 Fluid Property Values

Water			
Temperature°C	ρkg m^{-3}	σmN m^{-1}	νm^2 s^{-1} $\times 10^{-6}$
0	999.8395	75.64	1.787
4	999.9720	74.95	1.57
10	999.7026	74.23	1.307
15	999.1026	73.50	1.14
20	998.2071	72.75	1.004
25	997.0479	71.99	0.893
30	995.6502	72.10	0.801
40	992.2	69.6	0.658
60	983.2	66.24	0.475
80	971.8	62.67	0.365
100	958.4	48.91	0.29
Glycerol			
20 $\rightarrow$ 25	1261	64	718.42

Table A.2: Various values for the surface tension (σ), density(ρ), and viscosity(ν) values used for glycerol and water in the calculation [1][36][26][33].

Appendix B

Figures

B.1 Surface Tension to Density Fits Assuming Gravity $9.81\mathrm{m\,s^{-2}}$

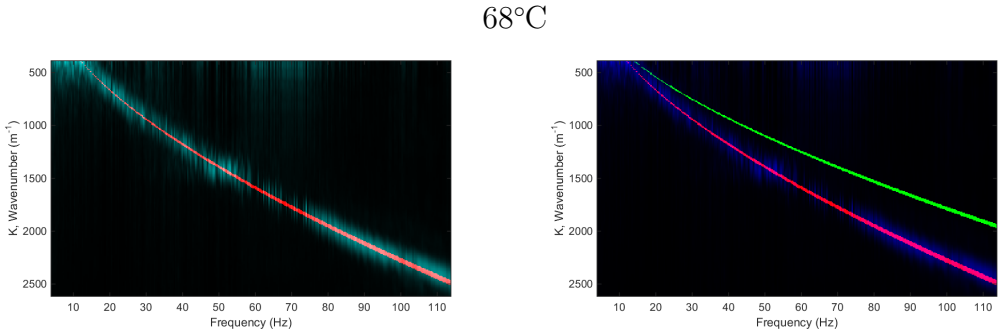

Figure B-1: The fit normalized match filter response at 68°C with the corresponding theoretical values.

63.2°C

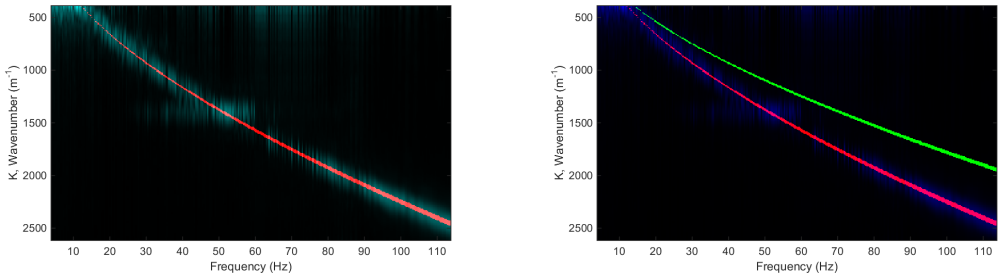

Figure B-2: The fit normalized match filter response at 63.2°C with the corresponding theoretical values.

58°C

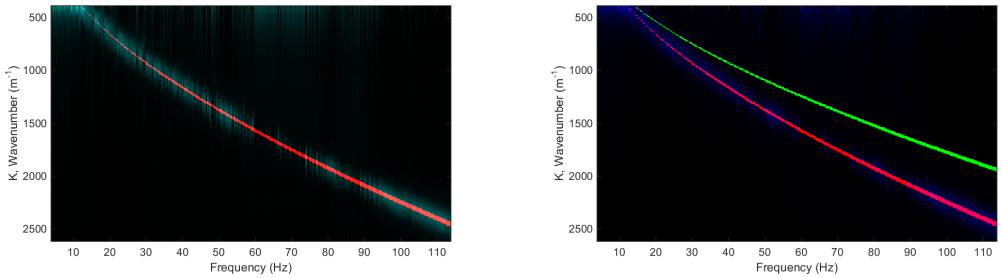

Figure B-3: The fit normalized match filter response at 58°C with the corresponding theoretical values.

53°C

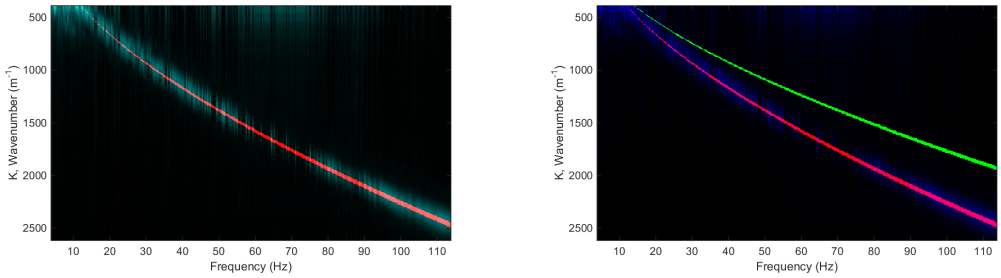

Figure B-4: The fit normalized match filter response at 53°C with the corresponding theoretical values.

46.5°C

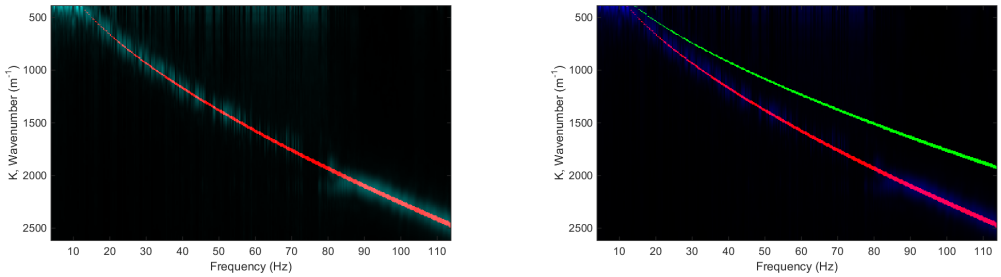

Figure B-5: The fit normalized match filter response at 46.5°C with the corresponding theoretical values.

42.9°C

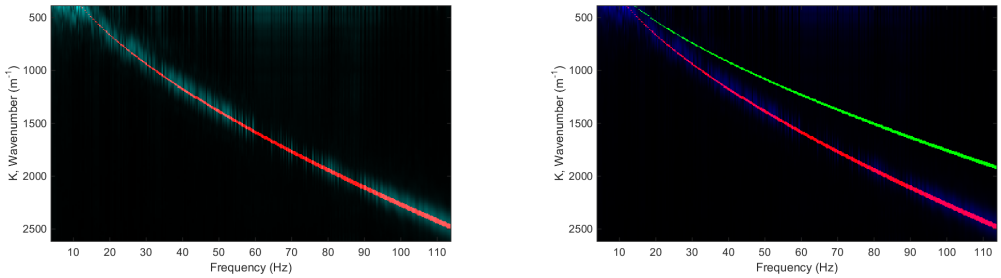

Figure B-6: The fit normalized match filter response at 42.9°C with the corresponding theoretical values.

37.6°C

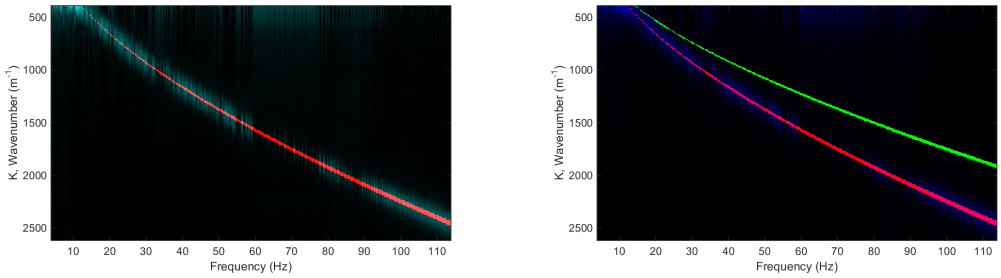

Figure B-7: The fit normalized match filter response at 37.6°C with the corresponding theoretical values.

33.1°C

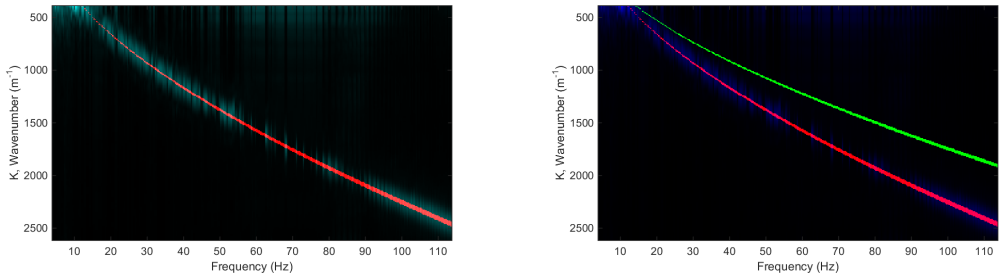

Figure B-8: The fit normalized match filter response at 33.1°C with the corresponding theoretical values.

27.8°C

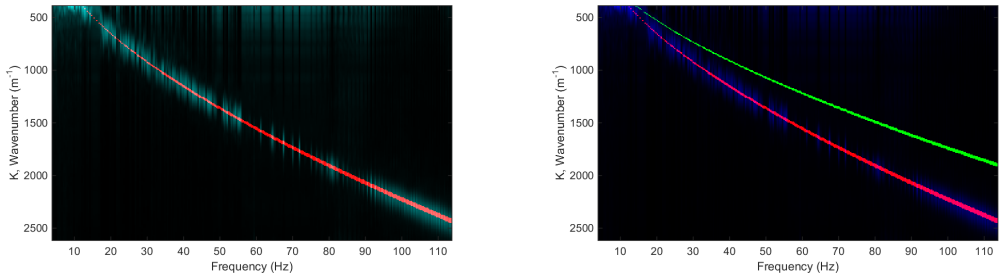

Figure B-9: The fit normalized match filter response at 27.8°C with the corresponding theoretical values.

Appendix C

Derivations

C.1 Group and Phase Velocity Ratios

$$v_g = \frac{3\frac{\sigma}{\rho}k^2 + g}{2\sqrt{gk + \frac{\sigma}{\rho}k^3}}$$

$$v_p = \frac{1}{k}\sqrt{gk + \frac{\sigma}{\rho}k^3}$$

$$k \to \text{inf}$$

$$v_p = \frac{3}{2}\left(\sqrt{\frac{\sigma}{\rho}}\right)$$

$$v_g = \sqrt{\frac{\sigma}{\rho}}$$

$$k \to \text{inf}$$

$$v_p = \sqrt{g}$$

$$v_g = \frac{1}{2}\sqrt{g}$$

C.2 Capillary–Gravity Wave FOV

$$
\begin{aligned}
\frac{\sigma}{\rho}k_0^3 &= gk_0 \\
\frac{\sigma}{\rho}k_0^2 &= g \\
k_0^2 &= \frac{\rho}{\sigma}g \\
k_0 &= \sqrt{\frac{\rho}{\sigma}g} \\
\frac{2\pi}{\lambda} &= \sqrt{\frac{\rho}{\sigma}g}
\end{aligned}
$$

$$
\lambda = \frac{2\pi}{\sqrt{\frac{\rho}{\sigma}g}} \tag{C.1}
$$

C.3 FOV Correction

$$
\begin{aligned}
\sigma_B &= \frac{w_{\sigma_B}f}{w_i} + f \\
w_{\sigma_T} &= \frac{w_i}{f}(\sigma_B - w_H - f) \\
w_{\sigma_T} &= \frac{w_i}{f}(\frac{w_{\sigma_B}f}{w_i} + f - w_H - f) \\
w_{\sigma_T} &= \frac{w_i}{f}(\frac{w_{\sigma_B}}{w_i}f - w_H)
\end{aligned}
$$

$$
w_{\sigma_T} = w_{\sigma_B} - \frac{w_i w_H}{f} \tag{C.2}
$$

Bibliography

[1] Release on the iapws formulation 2008 for the viscosity of ordinary water substance.

[2] The National Aeronautic and Atmospheric Administration's Gleen Research Center. Gas density gleen research center, 2014-06-12.

[3] Bob Atkins. Focus breathing.

[4] F Behroozi, J Smith, and W Even. Effect of viscosity on dispersion of capillary–gravity waves. *Wave Motion*, 48(2):176–183, 2011.

[5] Katherine L Bouman, Bei Xiao, Peter Battaglia, and William T Freeman. Estimating the material properties of fabric from video. In *Computer Vision (ICCV), 2013 IEEE International Conference on*, pages 1984–1991. IEEE, 2013.

[6] Leon Brillouin. *Wave propagation in periodic structures: electric filters and crystal lattices*. Courier Corporation, 2003.

[7] Matthieu Brizard, Mohamed Megharfi, E Mahe, and C Verdier. Design of a high precision falling-ball viscometer. *Review of Scientific Instruments*, 76(2):025109, 2005.

[8] PG Budny, PJ Regan, and AHN Roberts. The estimation of blood loss during burns surgery. *Burns*, 19(2):134–137, 1993.

[9] MR Cannon, RE Manning, and JD Bell. Viscosity measurement. kinetic energy correction and new viscometer. *Analytical Chemistry*, 32(3):355–358, 1960.

[10] Justin G Chen, Neal Wadhwa, Young-Jin Cha, Frédo Durand, William T Freeman, and Oral Buyukozturk. Structural modal identification through high speed camera video: Motion magnification. In *Topics in Modal Analysis I, Volume 7*, pages 191–197. Springer, 2014.

[11] Can Cinbis and BT Khuri-Yakub. A noncontacting technique for measuring surface tension of liquids. *Review of scientific instruments*, 63(3):2048–2050, 1992.

[12] Renato Cini, Giuseppe Loglio, and Augusta Ficalbi. Temperature dependence of the surface tension of water by the equilibrium ring method. *Journal of Colloid and Interface Science*, 41(2):287–297, 1972.

[13] LG Daignault, DC Jackman, and DP Rillema. A simple and inexpensive student viscometer. *Journal of Chemical Education*, 67(1):81, 1990.

[14] Abe Davis, Katherine L Bouman, Justin G Chen, Michael Rubinstein, Frédo Durand, and William T Freeman. Visual vibrometry: Estimating material properties from small motions in video. In *Proceedings of the IEEE Conference on Computer Vision and Pattern Recognition*, pages 5335–5343, 2015.

[15] Abe Davis, Michael Rubinstein, Neal Wadhwa, Gautham J Mysore, Fredo Durand, and William T Freeman. The visual microphone: Passive recovery of sound from video. *ACM Trans. Graph*, 33(4):79, 2014.

[16] Encyclopædia Britannica Online. Encyclopædia britannica.

[17] Encyclopædia Britannica Online. Encyclopædia britannica.

[18] Encyclopædia Britannica Online. Encyclopædia britannica.

[19] P Lecomte Du Noüy. A new apparatus for measuring surface tension. *The Journal of general physiology*, 1(5):521, 1919.

[20] P Lecomte du Noüy. An interfacial tensiometer for universal use. *The Journal of general physiology*, 7(5):625–631, 1925.

[21] W Stuart Edwards and S Fauve. Patterns and quasi-patterns in the faraday experiment. *Journal of Fluid Mechanics*, 278:123–148, 1994.

[22] Larry Hardesty. Phone-based laser rangefinder works outdoors.

[23] William D Harkins and Hubert F Jordan. Surface tension by the ring method. *Science*, 72(1855):73–75, 1930.

[24] Eugene Hecht and Alfred Zajac. Optics, addison, 1987.

[25] Website (Sky Light Holdings). Action camera shipments worldwide from 2010 to 2019 (in million unites).

[26] Joseph Kestin, Mordechai Sokolov, and William A Wakeham. Viscosity of liquid water in the range- 8 c to 150 c. *Journal of Physical and Chemical Reference Data*, 7(3):941–948, 1978.

[27] Horace Lamb. *Hydrodynamics*. Cambridge university press, 1932.

[28] Rui Li and Edward Adelson. Sensing and recognizing surface textures using a gelsight sensor. In *Proceedings of the IEEE Conference on Computer Vision and Pattern Recognition*, pages 1241–1247, 2013.

[29] James Lighthill. *Waves in fluids*. Cambridge university press, 2001.

[30] JF Padday, AR Pitt, and RM Pashley. Menisci at a free liquid surface: surface tension from the maximum pull on a rod. *Journal of the Chemical Society, Faraday Transactions 1: Physical Chemistry in Condensed Phases*, 71:1919–1931, 1975.

[31] Owen M Phillips. *The Dynamics of the Upper Ocean*. Cambridge University Press, 1977.

[32] Christopher J Seeton. Viscosity-temperature correlation for liquids. In *STLE/ASME 2006 International Joint Tribology Conference*, pages 131–142. American Society of Mechanical Engineers, 2006.

[33] John Bartlett Segur and Helen E Oberstar. Viscosity of glycerol and its aqueous solutions. *Industrial & Engineering Chemistry*, 43(9):2117–2120, 1951.

[34] Lisa Michelle Slaughter. Viscosity dependence of faraday wave formation thresholds. 2013.

[35] Antonio Torralba and William T Freeman. Accidental pinhole and pinspeck cameras: Revealing the scene outside the picture. In *Computer Vision and Pattern Recognition (CVPR), 2012 IEEE Conference on*, pages 374–381. IEEE, 2012.

[36] NB Vargaftik, BN Volkov, and LD Voljak. International tables of the surface tension of water. *Journal of Physical and Chemical Reference Data*, 12(3):817–820, 1983.

[37] Neal Wadhwa, Michael Rubinstein, Frédo Durand, and William T Freeman. Phase-based video motion processing. *ACM Transactions on Graphics (TOG)*, 32(4):80, 2013.

[38] Austin Weber. Automakers view cameras as essential safety devices.

[39] Tianfan Xue, Michael Rubinstein, Neal Wadhwa, Anat Levin, Fredo Durand, and William T Freeman. Refraction wiggles for measuring fluid depth and velocity from video. In *Computer Vision–ECCV 2014*, pages 767–782. Springer, 2014.